ISSN 1905-9094

GMSARN INTERNATIONAL JOURNAL

Vol. 2 No. 1
March 2008

Published by the

GREATER MEKONG SUBREGION ACADEMIC AND RESEARCH NETWORK
c/o Asian Institute of Technology
P.O. Box 4, Klong Luang, Pathumthani 12120, Thailand

GMSARN INTERNATIONAL JOURNAL

GMSARN MEMBERS

Asian Institute of Technology (AIT)	P.O. Box 4, Klong Luang, Pathumthani 12120, Thailand. www.ait.ac.th
Hanoi University of Technology (HUT)	No. 1, Daicoviet Street, Hanoi, Vietnam S.R. www.hut.edu.vn
Ho Chi Minh City University of Technology (HCMUT)	268 Ly Thuong Kiet Street, District 10, Ho Chi Minh City, Vietnam. www.hcmut.edu.vn
Institute of Technology of Cambodia (ITC)	BP 86 Blvd. Pochentong, Phnom Penh, Cambodia. www.itc.edu.kh
Khon Kaen University (KKU)	123 Mittraparb Road, Amphur Muang, Khon Kaen, Thailand. www.kku.ac.th
Kunming University of Science and Technology (KUST)	121 Street, Kunming P.O. 650093, Yunnan, China. www.kmust.edu.cn
National University of Laos (NUOL)	P.O. Box 3166, Vientiane Perfecture, Lao PDR. www.nuol.edu.la
Royal University of Phnom Penh (RUPP)	Russian Federation Blvd, PO Box 2640 Phnom Penh, Cambodia. www.rupp.edu.kh
Thammasat University (TU)	P.O. Box 22, Thamamasat Rangsit Post Office, Bangkok 12121, Thailand. www.tu.ac.th
Yangon Technological University (YTU)	Gyogone, Insein P.O. Yangon, Myanmar
Yunnan University	2 Cuihu Bei Road Kunming, 650091, Yunnan Province, China. www.ynu.edu.cn
Guangxi University	100, Daxue Road, Nanning, Guangxi, CHINA www.gxu.edu.cn

GMSARN
INTERNATIONAL JOURNAL

GREATER MEKONG SUBREGION ACADEMIC AND RESEARCH NETWORK (http://www.gmsarn.org)

The Greater Mekong Subregion (GMS) consists of Cambodia, China (Yunnan & Guanxi Provinces), Laos, Myanmar, Thailand and Vietnam.

The Greater Mekong Subregion Academic and Research Network (GMSARN) was founded followed an agreement among the founding GMS country institutions signed on 26 January 2001, based on resolutions reached at the Greater Mekong Subregional Development Workshop held in Bangkok, Thailand, on 10 - 11 November 1999. GMSARN is composed of eleven of the region's top-ranking academic and research institutions. GMSARN carries out activities in the following areas: human resources development, joint research, and dissemination of information and intellectual assets generated in the GMS. GMSARN seeks to ensure that the holistic intellectual knowledge and assets generated, developed and maintained are shared by organizations within the region. Primary emphasis is placed on complementary linkages between technological and socio-economic development issues. Currently, GMSARN is sponsored by Royal Thai Government.

The GMSARN member institutions are the Asian Institute of Technology; the Institute of Technology of Cambodia; Kunming University of Science and Technology, Yunnan Province, China; National University of Laos; Yangon Technological University, Myanmar; Khon Kaen University, Thailand; Thammasat University, Thailand; Hanoi University of Technology, Vietnam; Ho Chi Minh City University of Technology, Vietnam; the Royal University of Phnom Penh in Cambodia, and Yunnan University in Yunnan Province, China.

GMSARN International Journal

Volume 2, Number 1, March 2008

CONTENTS

Multi-Objective Optimal Power Flow Considering System Emissions and Fuzzy Constraints

Keerati Chayakulkheeree and Weerakorn Ongsakul

Abstract*— *This paper proposes a fuzzy multi-objective optimal real power flow (FMOPF) with transmission line limit and transformer loading constraints. In the proposed FMOPF algorithm, the total system operating cost, total system SO_2, NO_x, and CO_2 emissions fuzzy minimization objectives are solved simultaneously considering fuzzy line flow constraints, using fuzzy linear programming (FLP). The proposed FMOPF is tested with the IEEE 30 bus system. The simulation results shown that the proposed FMOPF can efficiently and effectively trade off among total system operating cost and total system SO_2, NO_x, and CO_2 emissions.

***Keywords*— Optimal power flow, emission power dispatch, fuzzy linear programming.**

1. INTRODUCTION

In power system operation, optimal power flow (OPF) is an extended problem of economic dispatch (ED) to include several parameters such as; generator voltage, transformer tap change, SVC, and include constraints such as; transmission line and transformer loading limits, bus voltage limit, stability margin limit. The objectives may be; minimum generation cost, minimum transmission loss, minimum deviation from target schedule, minimum control shift to alleviate violation, minimum emission. Current interest in the OPF centers around its ability to solve for large scale power system optimal solution that takes account of more objectives, parameter, and constraints of the system.

The main purpose of optimal power dispatch is to minimize the operating cost of the power system satisfying power balance constraints. However, the operating cost minimization objective may not necessarily be the best in term of environment. Several alternatives for achieving emission reductions include adding gas cleaner, switching fuel to low sulfur fuel, and adopting new power dispatch. Among these methods, the power dispatch approach is preferred because it is easily implemented and requires minimum additional costs [1]. Therefore, the unit dispatch considering emission beside cost minimization has received widespread attention for effective short-term option with smaller capital outlay [1-6]. The major environmental concerns in optimal power dispatch include emission of SO_2 [1-2, 4-6], NO_x [2-6], and CO_2 [5].

In practical power system operation, the single objective such as total operating cost minimization may not be directly applied, since it may lead to unsatisfactory of other aspects such as system security, fuel security, environmental concern. In addition, constraints in conventional OPF are usually given fixed values that have to be met which may lead to over-conservative solutions. When the solution violates the inequality constraints, it is difficult to decide which constraint should be relaxed and the extent of relaxation. Therefore, in the system operator view point, certain trade-off among several objectives and constraints would be desirable rather than a single rigid minimum or maximum solution.

Techniques for treating emission in optimal power dispatch have formed of two major research directions. Many techniques treated the emission as constraints [1, 2, 4]. However, due to the conflicting and non-commensurable nature of operating cost and emission, the earlier techniques formulated the problem to combine emissions minimization in to the total operating cost minimization problem [3, 5, 7]. In [5] and [7], the emission minimization objectives were combined into the total cost minimization objective by weighting methods. Nevertheless, in the absence of sufficient information, defining the weighting factors or equivalent cost of emission is incredibly difficult. In [3], the bi-objective power dispatch using fuzzy satisfaction-maximizing decision approach was proposed. Nonetheless, the problem included only minimum NO_x emission and total operating cost objectives with the linear fuzzy membership function.

This paper proposes the fuzzy multi-objective optimal real power flow (FMOPF) for selecting a final compromise solution for operating cost and emissions minimization problems. In the proposed FMOPF algorithm, the total system operating cost, total system SO_2, NO_x, and CO_2 emissions fuzzy minimization objectives are solved simultaneously using fuzzy linear programming (FLP). The proposed FMOPF is tested with the IEEE 30 bus system. The simulation results shown that the proposed FMOPF can efficiently and effectively trade off among total system operating cost and total system SO_2, NO_x, and CO_2 emissions.

The organization of this paper is as follows. Section 2

Assist. Prof. Dr. Keerati Chayakulkheeree (corresponding author) is with Department of Electrical Engineering, Faculty of Engineering, Sripatum University, 61 Phaholyotin Rd., Senanikom, Jatujak, Bangkok, 10900, Thailand. Phone: 66-2-579-1111 ext 2272; Fax: 66-2-579-1111 ext 2147; E-mail: keerati.ch@spu.ac.th.

Assoc. Prof. Dr. Weerakorn Ongsakul is with Energy Field of Study, Asian Institute of Technology, P.O. Box 4, Klong Luang, Pathumthani 12120, Thailnad. E-mail: ongsakul@ait.ac.th.

addresses the FMOPF problem formulation. The FLP for FMOPF problem is given in Section 3. Numerical results on the IEEE 30 bus test system are illustrated in Section 4. Lastly, the conclusion is given.

2. MOPF PROBLEM FORMULATION

Consider the fact that real power injected at a bus does not change significantly for a small change in the magnitude of bus voltage and the reactive power injected at a bus does not change for a small change in the phase angle of bus voltage. Therefore, the bus voltage magnitudes and transformer tap changes are not included in the total operating cost and emissions multi-objective fuzzy minimization subproblem. Similarly, the real power generations are not included in the total real power loss fuzzy minimization subproblem.

2.1 Total operating cost and emissions multi-objective fuzzy minimization subproblem

The operating cost of the generating unit is expressed as the sum of polynomial function of the real power generation of the unit. Therefore, objective is to minimize total system operating cost,

$$FC = \sum_{i \in BG} F(P_{Gi}) \tag{1}$$

The environment aspect cover a myriad of air quality concerns including control of power plant emissions of constituents of acid rain specifically sulfur dioxide (SO_2) and oxide of nitrogen (NO_x). The carbon dioxide (CO_2) emission is also taken into account since it is considered as a global warming gas.

The emission functions for the unit *i* can be expressed as polynomial function of real power generation of the unit. Therefore, the addition objective functions are minimize total NO_x emission,

$$EC_{NO_x} = \sum_{i \in BG} E_{NO_x}(P_{Gi}), \tag{2}$$

and minimize total SO_2 emission,

$$EC_{SO_2} = \sum_{i \in BG} E_{SO_2}(P_{Gi}), \tag{3}$$

and minimize total CO_2 emission,

$$EC_{CO_2} = \sum_{i \in BG} E_{CO_2}(P_{Gi}). \tag{4}$$

subject to the power balance constraints,

$$P_{Gi} - P_{Di} = \sum_{j=1}^{NB} |V_i||V_j||y_{ij}| \cos(\theta_{ij} - \delta_{ij}), i = 1,..., NB, \tag{5}$$

$$Q_{Gi} - Q_{Di} = -\sum_{j=1}^{NB} |V_i||V_j||y_{ij}| \sin(\theta_{ij} - \delta_{ij}), i = 1,..., NB, \tag{6}$$

and the line flow limit and transformer loading constraints,

$$|f_l| \tilde{\leq} f_l^{\max}, \text{ for } l=1, \ldots, NL, \tag{7}$$

and fuzzy generator ramprate constraint,

$$P_{Gi}^o - R_{Gi}^{dec} \cdot Min \tilde{\leq} P_{Gi} \tilde{\leq} P_{Gi}^o - R_{Gi}^{inc} \cdot Min, \; i = 1,\ldots, NR, \tag{8}$$

and the generator minimum and maximum operating limit constraints,

$$P_{Gi}^{\min} \leq P_{Gi} \leq P_{Gi}^{\max}, \; i \in BG. \tag{9}$$

2.2 Real power loss fuzzy minimization subproblem

To minimize the total real power loss, the total real power loss minimization subproblem is solved iteratively with the total fuel cost fuzzy minimization subproblem. The objective is formulated as,

$$\text{Minimize } \Delta P_{loss} = \left[\frac{\mathbf{dP_{loss}}}{\mathbf{d|V|}} \; \frac{\mathbf{dP_{loss}}}{\mathbf{dT}}\right] \begin{bmatrix} \mathbf{\Delta|V|} \\ \mathbf{\Delta T} \end{bmatrix}, \tag{10}$$

subject to the fuzzy bus voltage limits constraints,

$$\Delta|V_i^{\min}| \tilde{\leq} \Delta|V_i| \tilde{\leq} \Delta|V_i^{\max}|, \text{ for } i = 1,\ldots, NV, \tag{11}$$

where

$$\Delta|V_i^{\min}| = |V_i^{\min}| - |V_i|, \text{ for } i = 1,\ldots, NV, \tag{12}$$

$$\Delta|V_i^{\max}| = |V_i^{\max}| - |V_i|, \text{ for } i = 1,\ldots, NV, \tag{13}$$

and the transformer tap-change limits constraints,

$$\Delta T_i^{\min} \leq \Delta T_i \leq \Delta T_i^{\max}, \text{ for } i = 1,\ldots, NT, \tag{14}$$

where

$$\Delta T_i^{\min} = T_i^{\min} - T_i, \text{ for } i = 1,\ldots, NT, \tag{15}$$

$$\Delta T_i^{\max} = T_i^{\max} - T_i, \text{ for } i = 1,\ldots, NT, \tag{16}$$

$$Q_{Gi}^{\min} \leq Q_{Gi} \leq Q_{Gi}^{\max}, \; i \in BG. \tag{17}$$

$|V_i|$, $i \in BG$, and T_i, $i = 1,\ldots,NT$, are the unknown control variables obtained from the total real power loss fuzzy minimization subproblem.

P_{Gi}, where $i \in BG$, is the output of the FMOPF algorithm. The method is intended to line flow and transformer loading limits constrained economic dispatch in power system. The bus voltages and reactive power optimal controls are not included in the paper.

3. FUZZY LINEAR PROGRAMMING ALGORITHM FOR FMOPF PROBLEM

To solve the FMOPF problem, the goal of decision-maker can be expressed as a fuzzy set and the solution space is defined by constraints that can be modeled by fuzzy set [8]. The multi-objective fuzzy minimization subproblem of the proposed FMOPF can be formulated as,

$$\text{Maximize } \min\{\mu_1(x), \mu_2(x), \mu_3(x), \mu_4(x)\}, \quad (9)$$

$$\text{subject to } \mathbf{B}\cdot\mathbf{P_{Gi}} \lesssim \mathbf{d} \quad (10)$$

and power balance constraints in (2) and (3), crisps inequality line flow limit and transformer loading constraints in (7), and low and high limits of P_{Gi} in (8).

$\mathbf{P_{Gi}}$ is the column matrix representing the set of real power generation of the generator connected to bus *i*. **d** is the vector representing of fuzzy objective functions in Eqs. (1)-(4). Each row of **B** in (10) is represented by a fuzzy set with the membership functions of $\mu_i(x)$. $\mu_i(x)$ can be interpreted as the degree to which $\mathbf{P_{Gi}}$ satisfies the fuzzy objective function. Here, $\mu_1(x)$ is the degree of satisfaction of $\mathbf{P_{Gi}}$ for the objective function, whereas $\mu_2(x)$ to $\mu_4(x)$ are the degrees of satisfactions of $\mathbf{P_{Gi}}$ for the, total system NO_x, SO_x, and CO_2 emissions, respectively. In this paper, the hyperbolic function is used to represent the nonlinear, S-shaped, membership function [9]. The function can be expressed as,

$$\mu_i(x) = \frac{1}{2}\cdot\tanh\left(\left(\mathbf{B_i}\cdot\mathbf{P_{Gij}} - \frac{\alpha_i+\beta_i}{2}\right)\cdot\gamma_i\right)+\frac{1}{2}\cdot \quad (11)$$

where α_i, β_i, and γ_i are the parameters representing the shape of $\mu_i(x)$ depending on the decision maker and $\mathbf{B_i}$ is the row *i* of **B**.

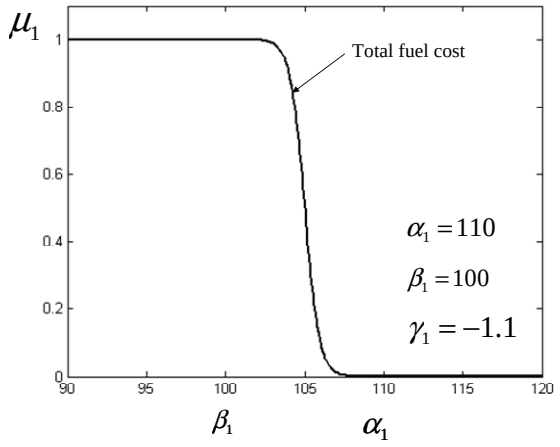

Fig. 1. Membership function for total operating cost.

The fuzzy linear programming approach translates the multiple objectives into additional constraints by assigning membership function to each objective. Due to complexity in computation, many literatures set the parameters by heuristics based on operators' intuition. In this paper, the parameters were set by the worst case principle, which is based on the concept that none of the objective functions can be reduced any further by increasing other objective functions. This can reflect the optimal trade off among the objectives.

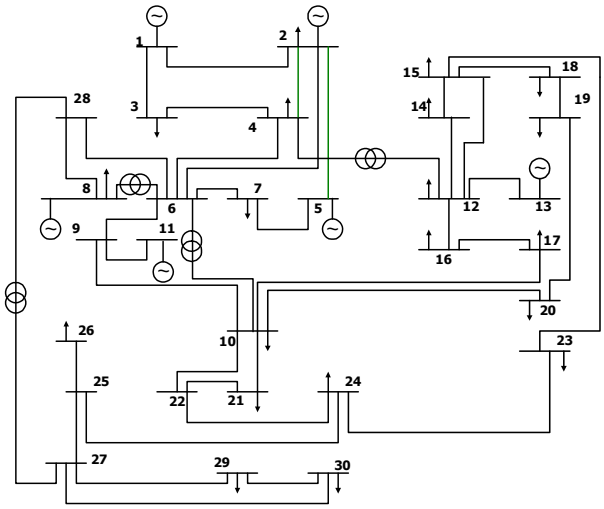

Fig. 2. IEEE 30 bus test system network diagram.

Therefore, to obtain the membership function of objective function, α_1 is the minimum total operating cost solved by the LP without consideration of emissions. On the other hand, β_1 is the maximum total fuel cost among the solution of minimization of other fuzzy objective functions. γ_1 is obtained by α_1/β_1. Similarly, α_2, α_3, and α_4 are the minimum SO_2, NO_x, and CO_2 emissions solved by the LP without consideration of total fuel cost and each other fuzzy objective functions. β_2, β_3, and β_4 are the maximum NO_x, SO_2, and CO_2 emissions among the solution of minimization of the total fuel cost and each other fuzzy objective functions.

Table 1. The generator fuel cost function

Gen bus	Min (MW)	Max (MW)	$F(P_{Gi}) = a_i\cdot P_{Gi}^3 + b_i\cdot P_{Gi}^2 + c_i\cdot P_{Gi} + d_i$			
			a_i	b_i	c_i	d_i
1	50	200	0.0010	0.092	14.5	-136
2	20	80	0.0004	0.025	22	-3.5
5	15	50	0.0006	0.075	23	-81
8	10	50	0.0002	0.1	13.5	-14.5
11	10	50	0.0013	0.12	11.5	-9.75
13	12	40	0.0004	0.084	12.5	75.6

With the defined membership functions of objective function and fuzzy constraints, the fuzzy optimization problem can be reformulated as,

$$\text{Maximize } \mu', \quad (12)$$

$$\text{subject to } \mu' \le \mu_i(x), \text{ for } i = 1,\ldots, 4, \quad (13)$$

Table 2. The SO_2, NO_x, and CO_2 emissions functions

$$E_{SO_2}(P_{Gi}) = a_{SO_2 i} \cdot P_{Gi}^3 + b_{SO_2 i} \cdot P_{Gi}^2 + c_{SO_2 i} \cdot P_{Gi} + d_{SO_2 i}$$
$$E_{NO_x}(P_{Gi}) = a_{NO_x i} \cdot P_{Gi}^3 + b_{NO_x i} \cdot P_{Gi}^2 + c_{NO_x i} \cdot P_{Gi} + d_{NO_x i}$$
$$E_{CO_2}(P_{Gi}) = a_{CO_2 i} \cdot P_{Gi}^3 + b_{CO_2 i} \cdot P_{Gi}^2 + c_{CO_2 i} \cdot P_{Gi} + d_{CO_2 i}$$

Gen bus	SO_2				NO_x				CO_2			
	$a_{SO_2 i}$	$b_{SO_2 i}$	$c_{SO_2 i}$	$d_{SO_2 i}$	$a_{NO_x i}$	$b_{NO_x i}$	$c_{NO_x i}$	$d_{NO_x i}$	$a_{CO_2 i}$	$b_{CO_2 i}$	$c_{CO_2 i}$	$d_{CO_2 i}$
1	0.0005	0.150	17.0	-90.0	0.0012	0.052	18.5	-26.0	0.0015	0.092	14.0	-16.0
2	0.0014	0.055	12.0	-30.5	0.0004	0.045	12.0	-35.0	0.0014	0.025	12.5	-93.5
5	0.0010	0.035	10.0	-80.0	0.0016	0.050	13.0	-15.0	0.0016	0.055	13.5	-85.0
8	0.0020	0.070	23.5	-34.5	0.0012	0.070	17.5	-74.0	0.0012	0.010	13.5	-24.5
11	0.0013	0.120	21.5	-19.75	0.0003	0.040	8.5	-89.0	0.0023	0.040	21.0	-59.0
13	0.0021	0.080	22.5	25.6	0.0014	0.024	15.5	-75.0	0.0014	0.080	22.0	-70.0

and $0 \le \mu' \le 1$, (14)

and power balance constraints in (2) and (3), crisps inequality line flow limit and transformer loading constraints in (7), and low and high limits of P_{Gi} in (8).

The FLP computational procedure is as follow,

Step 1: Solve the linear programming for individual objective function in Eqs. (1)-(4)

Step 2: Compute individual objective value of each case.

Step 3: Obtain α_i and β_i from the minimum and maximum of all objective values computed in step 2.

Step 4: Solve the fuzzy linear programming of multi-objective problem using α_i and β_i from step 3.

4. SIMULATION RESULTS

The IEEE 30 bus system is used as the test data. It network diagram is shown in Fig.2. The generator fuel cost, and SO2, NOx, and CO2 emissions functions are given in Tables 1 and 2. The generator fuel cost, and SO2, NOx, and CO2 emissions functions are linearized in to 5 piece-wise linear functions.

Table 3. Dispatch results of minimum total operating cost condition

```
---------------------------
** ** Generation Cost ** **
---------------------------
 BUS       P_GEN          Cost         Inc-Cost
            (MW)         ($/h)         ($/MWh)
  1        50.00       944.00015       21.60000
  2        68.00      1733.87260       25.54960
  5        36.00       872.19306       26.47760
  8        50.00       935.49803       18.99999
 11        43.07       812.15973       19.08103
 13        40.00       735.59962       16.50000
Total Cost = 6033.32319 $/h
Total SO2  = 7035.94301 ton/h
Total NOX  = 5060.62788 ton/h
Total CO2  = 5917.43863 ton/h
```

Tables 3-6 address the dispatch results of minimum operating cost, SO_2 emission, NO_x emission, and CO_2 emission, respectively. Table 7 shows the dispatch results of the FMOPF result. The results show that the sigle objective approaches result in the inferior results in the others objective and less degree of satisfaction.

Table 4. Dispatch results of minimum SO_2 emission condition

```
---------------------------
** ** Generation Cost ** **
---------------------------
 BUS       P_GEN          Cost         Inc-Cost
            (MW)         ($/h)         ($/MWh)
  1        50.00       944.00013       21.60000
  2        68.00      1733.87267       25.54960
  5        50.00      1331.49953       28.25000
  8        36.68       625.17418       17.43752
 11        42.00       781.24482       18.83320
 13        40.00       735.59969       16.50000
Total Cost = 6151.39102 $/h
Total SO2  = 6709.76760 ton/h
Total NOX  = 5009.04237 ton/h
Total CO2  = 5976.29335 ton/h
```

Table 5. Dispatch results of minimum NO_x emission condition

```
---------------------------
** ** Generation Cost ** **
---------------------------
 BUS       P_GEN          Cost         Inc-Cost
            (MW)         ($/h)         ($/MWh)
  1        50.00       944.00000       21.60000
  2        69.86      1791.70996       25.69841
  5        43.00      1094.37920       27.33440
  8        34.00       567.96080       17.13120
 11        50.00      1027.75000       20.75000
 13        40.00       735.60000       16.50000
Total Cost = 6161.39996 $/h
Total SO2  = 6874.94078 ton/h
Total NOX  = 4897.48710 ton/h
Total CO2  = 6104.20084 ton/h
```

The comparison on the results with total cost minimization, SO2 minimization, NOx Minimization, CO2 minimization, and the proposed FMOPF is shown in Fig.3.

In this test case, the minimum operating cost solution results in the highest SO2 emission of 7035.94 ton/h. Meanwhile, the minimum NOx emission results in the highest total operating cost and CO2 emissions, of

6161.4 $/h and 6104.2 ton/h, respectively and the minimum CO2 solution results in the highest NOX emission of 5187.67 ton/h.

In contrast, the proposed FMOPF is effectively trades off all objectives in the fuzzy reasoning sense leading to the most compromise solution. Note the FMOPF results in the degree of satisfaction (μ') of 0.881.

Table 6. Dispatch results of minimum CO_2 emission condition

```
---------------------------
** ** Generation Cost ** **
---------------------------
 BUS       P_GEN          Cost         Inc-Cost
            (MW)         ($/h)         ($/MWh)
  1        50.00       943.99989       21.60000
  2        68.00       1733.87299      25.54960
  5        50.00       1331.50050      28.25000
  8        50.00       935.50167       19.00001
 11        34.00       571.06491       17.08280
 13        34.68       626.79931       15.89414
Total Cost = 6142.73928 $/h
Total SO2  = 6766.27879 ton/h
Total NOX  = 5187.67201 ton/h
Total CO2  = 5805.99644 ton/h
```

Table 7. Dispatch results of the proposed FMOPF

```
---------------------------
** ** Generation Cost ** **
---------------------------
 BUS       P_GEN          Cost         Inc-Cost
            (MW)         ($/h)         ($/MWh)
  1        49.98       943.48013       21.59680
  2        63.29      1590.34897       25.18430
  5        44.74      1151.97467       27.55687
  8        45.35       822.01699       18.44621
 11        43.82       833.92697       19.25416
 13        39.56       726.39639       16.44944
Total Cost = 6068.14412 $/h
Total SO2  = 6822.92570 ton/h
Total NOX  = 5018.07405 ton/h
Total CO2  = 5889.96324 ton/h
```

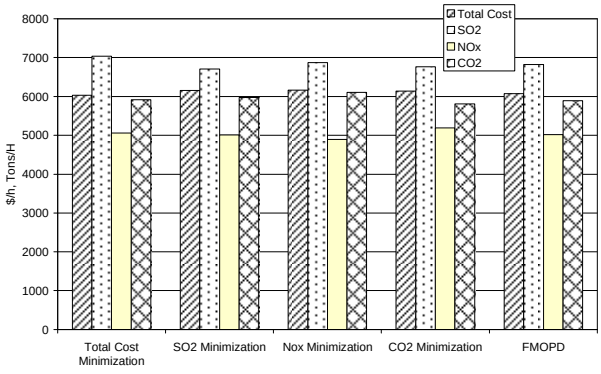

Fig. 3. The comparison on the results with different objective functions.

5. CONCLUSIONS

In this paper, a fuzzy multi-objective optimal real power flow (FMOPF) with transmission line limit and transformer loading constraints is successfully trading off between the total system operating cost, SO_2 emission, NO_x emission, and CO_2 emission, satisfying transmission line limits and transformer loading constraints. The proposed FMOPF results in a compromise solution and can potentially be applied to overcome the difficulties of obtaining the weight or equivalent cost of emission.

ACKNOWLEDGMENT

This work was supported by Sripatum University.

NOMENCLATURE

Known Variables

EC_{NO_x}, EC_{SO_x}, and EC_{CO_2}: the total system NO_x, SO_x, and CO_2 emissions, respectively (ton/h),

$E_{NO_x}(P_{Gi})$, $E_{SO_x}(P_{Gi})$, and $E_{CO_2}(P_{Gi})$: the NO_x, SO_2, and CO_2 emissions of the generator connected to bus *i*, respectively (ton/h),

$F(P_{Gi})$: the operating cost of the generator connected to bus *i* ($/h),

BG : set of buses connected with generators

$f_l^{\max}$: MVA flow limit of line or transformer *l* (MVA)

NB : total number of buses

NT : total number of on load tap-changing transformers

P_{Di} : total real power demand at bus *i* (MW)

$P_{Gij}^{\max}$: real power generation of the linearized cost function segment *j* of generator at bus *i* (MW)

$P_{Gij}^{\max}$: maximum real power generation of the linearized cost function segment *j* of generator at bus *i* (MW)

$P_{Gi}^{\max}$: maximum real power generation at bus *i* (MW)

$P_{Gi}^{\min}$: minimum real power generation at bus *i* (MW)

Q_{Di} : reactive power demand at bus *i* (MVAR)

$Q_{Gi}^{\max}$: maximum reactive power generation at bus *i* (MW)

$Q_{Gi}^{\min}$: minimum reactive power generation at bus *i* (MW)

R_{Gi}^{inc} : ramping rate limit of generator *i* when increasing real power generation (MW/min)

R_{Gi}^{dec} : ramping rate limit of generator *i* when decreasing real power generation (MW/min)

Min : time interval in minute (min)

S_{ij} : linearized incremental cost segment *j* of generator at bus *i* ($/MWh)

$T_i^{\max}$: maximum tap setting of transformer *i* (MW)

$T_i^{\min}$: minimum tap setting of transformer *i* (MW)

$|V_i^{\max}|$: maximum voltage magnitude at bus *i* (kV)

$|V_i^{\min}|$: minimum voltage magnitude at bus *i* (kV)

$|y_{ij}|$: magnitude of the y_{ij} element of Y_{bus} (mho)

θ_{ij} : angle of the y_{ij} element of Y_{bus} (radian)

Unknown Control Variables

P_{Gi} : the real power generation of the generator

connected to bus *i* (MW),

T_i : tap setting of transformer *i* (MW)

$|V_i|$: generator voltage magnitude at bus *i*, $i \in BG$ (kV)

State and Output Variables

FC : total system fuel cost ($/h)

f_l : MVA flow of line or transformer *l* (MVA)

NC : total number of line flow and transformer loading constraints

NR : total number of generator ramprate constraints

NV : total number of bus voltage magnitude constraints

P_i : injection real power at bus *i* (MW)

P_{loss} : total system real power loss (MW)

Q_{Gi} : reactive power generation at bus *i* (MVAR)

$|V_i|$: voltage magnitude at load bus *i*, $i \notin BG$ (kV)

δ_{ij} : voltage angle difference between bus *i* and *j* (radian)

REFERENCES

[1] Yong-Lin Hu and William G. Wee. 1994. A Hierarchical System for Economic Dispatch with Environmental Constrains. *IEEE Trans. Power Syst.*, 9(2): 1076-1082.

[2] R. Ramanathan. 1994. Emission Constrained Economic Dispatch. *IEEE Trans. Power Syst.*, 9(4): 1994-2000.

[3] Chao-Ming Huang, H. T. Yang, and C. L. Huang. 1997. Bi-Objective Power Dispatch Using Fuzzy Staisfaction-Maximizing Decision Approach. *IEEE Trans. Power Syst.*, 12(4): 1715-1721.

[4] Victoria L. Vickers, Walter J.Hobbbs, Suri Vemuri and Daniel L.Todd. 1994. Fuel Resource Scheduling With Emission Constraints. *IEEE Trans. Power Syst.*, 9(3): 1531-1538.

[5] Chao-Ming Huang and Yann-Chang Huang. 2003. A Novel Approach to Real-Time Economic Emission Power Dispatch. *IEEE Trans. Power Syst.*, 18(1): 288-294.

[6] J. H. Talaq, Ferial and M.E. El-Hawary. 2003. Minimum Emission power Flow. *IEEE Trans. Power Syst.*, 9(1): 429-435.

[7] P. Venkatesh, R. Gnanadass and Narayana Prasad Padhy. 2003. Comparison and Application of Evolutionary Programming Techniques to Combined Economic Emission Dispatch with Line Flow Constraints. *IEEE Trans. Power Syst.*, 18(2): 688-697.

[8] H. J. Zimmermann. 1987. *Fuzzy Sets, Decision Making, and Expert Systems*. Boston: Kluwer Academic Publishers,

[9] K. Chayakulkheeree and W. Ongsakul, 2005. Fuzzy Constrained Optimal Power Dispatch for Electricity and Ancillary Services Markets. *Electric Power Components and Systems*, 33(4).

Control Performance of a MPPT controller with Grid Connected Wind Turbine

K. Krajangpan, B. Neammanee and S. Sirisumrannukul

Abstract*— *The key issue of wind energy conversion systems is how to efficiently operate the wind turbines. This issue relies on the location where the turbines are operated. In addition, the control system with respect to machine operation and power production is essential in order to extract power from the turbines as much as possible regardless of wind speed. The control performance of a MPPT controller with a grid connected wind turbine is therefore proposed in this paper with two objectives. The first objective is to maximize the output power from the wind turbine by the maximum peak power tracking (MPPT) method. The second objective focuses on the output power from a DC generator directly coupled to the grid via a DC/AC converter or line side converter. Experiments are conducted with a 7.5kW grid connected system, using step wind speeds and a real wind speed data set from a site in a southern province of Thailand as the input of a wind simulator. The experimental results can confirm good MPPT performance and low harmonic distortion in the grid connected line side converter.

***Keywords*— Maximum peak power tracking, MPPT, wind energy conversion, grid connected.**

1. INTRODUCTION

As the impact of climate change has become public concern and the security of energy procurement is an issue, wind has become one of the fastest growing energy sources and is expected to continue growing in the electricity supply industry. The key issue of wind energy conversion systems is how to efficiently operate the wind turbines. This issue relies on the location where the turbines are operated. That is, the wind turbines should be placed where wind speed is strong and reasonably constant. In addition, the control system with respect to machine operation and power production is essential in order to extract power from the turbines as much as possible.

In general, a wind turbine is mechanically designed to produce its rating at a certain wind speed which is referred as rated wind speed. For wind speeds below the rated one, the main task of a controller is to capture the maximum power output. This task can be achieved by the maximum peak power tracking (MPPT) method.

References [1-3] propose a MPPT technique to track the maximum peak power without wind turbine characteristics. However, types of load are not considered. References [4, 5] implement controllers for grid connection via a line side converter and a transformer. The result is impressive in that active and reactive power can be directly and separately controlled with power factor near unity but the DC input source is not taken into account. It is therefore proposed in this paper a MPPT-based technique with consideration of grid connection. The developed controller has two main objectives. [9-10]

The first objective is to maximize the output power from a wind turbine by the MPPT method. The second objective focuses on the output power from a DC generator coupled with a boost type converter to increase the DC bus voltage and directly coupled to the grid via a DC/AC converter or line side converter. Experiments are conducted with a 7.5kW grid connected system, using step wind speeds, variable wind speeds and a real wind speed data set from a site in a southern province of Thailand as the input of a wind simulator.

2. SYSTEM DESCRIPTION

A MPPT controller with a grid connected wind turbine is shown in Fig. 1. The system composed of three parts. The first part is the wind turbine coupled with a gear box and a DC generator. The wind turbine captures the energy from the wind and increases speed by the gear box to match speed of the generator. The second part is the MPPT controller composed of a power unit and control unit. The power unit consists of a boost converter which has two main functions. The first function is to amplify the DC link voltage to obtain enough voltage to match that of a 7.5 kW line side converter. The second function is to control the DC-bus output voltage for power flow control from the wind turbine to the grid to obtain the maximum peak power. The last part is a 7.5kW line side converter working as the front end of this system. The main function of the line side converter is to flow the energy production from the system to the three phase grid with a power factor of near unity. The lower part of the figure is a control unit consisting of the developed the MPPT controller, a data acquisition system and a line side converter controller. The MPPT controller receives the rotational speed form a rotary encoder, currents and voltages. The MPPT then builds a control command and sends it to the boost converter.

K. Krajangpan, B. Neammanee (corresponding author) and S. Sirisumrannukul are with Department of Electrical Engineering, King Mongkut's Institute of Technology North Bangkok 1518 Bangsue, Bangkok 10800, Thailand. Phone: (+66)2913-2500-24 Ext: 8420; Fax: (+66)2585-7350; E-mail: bln@kmutnb.ac.th.

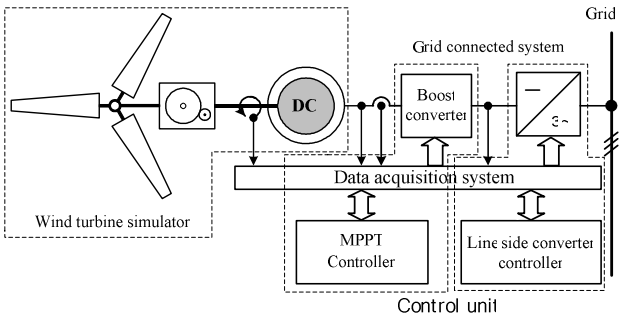

Fig. 1. MPPT controller with grid connected system for wind turbine.

2.1 Wind Turbine Characteristics

In order to describe wind turbine control schemes, a brief review of wind turbine characteristics is given here. The wind turbine characteristics are generally governed by (1) to (5).

$$T_a - T_e = J\frac{d\omega}{dt} + B\omega \tag{1}$$

$$P_a - P_e = \omega J\frac{d\omega}{dt} + B\omega^2 \tag{2}$$

$$P_a = P_W C_P(\lambda) = \frac{1}{2}\rho A v^3 C_P(\lambda) \tag{3}$$

$$\frac{1}{2}\rho A v^3 C_P(\lambda) - \eta P_{out} = \omega J\frac{d\omega}{dt} \tag{4}$$

$$\lambda = \frac{\omega R}{v} \tag{5}$$

Equation (3) reveals that the power coefficient C_P is a function of tip-speed ratio λ, which is defined by Equation (5). The C_P - λ relationship is graphically shown in Fig. 2. This figure is obtained from a real 3 kW horizontal axis wind turbine. The goal of control schemes for maximum wind power extraction is to keep wind turbine operating at their optimal tip-speed ratio, where the maximum energy conversion efficiency of wind turbine can be reached. In Figure 3, $C_P^{\max}$ is 0.4. In order to simplify the following discussion, the parameter η in (4) is assumed to be unity. Therefore, P_e is equal to P_{out}.

The power coefficient characteristic of a wind turbine has a single maximum at a specific value of the tip speed ratio. When the rotor operates at constant speed, the power coefficient will be maximum at only one wind speed. To achieve the highest annual energy capture, the value of the power coefficient must be maintained at the maximum level all the time, regardless of the wind speed [4]. For this reason, maximizing energy capture is to keep operating points at $(\lambda_0, c_P^{\max})$ of Fig. 2.

Figure 3 shows a power-rotational speed curve with seven different wind speeds ($\upsilon_1, \upsilon_2, \ldots, \upsilon_7$). Path A-B in the figure represents the optimum tracking path on which each operating point has $C_P^{\max}$ to build a rotational speed reference command, ω_{ref}, for the controller.

$$\omega_{ref} = \sqrt{T_a / k_T} \tag{6}$$

where

$$T_a = \frac{\rho}{2}\pi R^5 c_P^{\max}\frac{1}{\lambda_o^3}\omega_t^2 = k_T\omega_{ref}^2 \tag{7}$$

$$k_T = \frac{\rho}{2}\pi R^5 c_P^{\max}\frac{1}{\lambda_o^3} \tag{8}$$

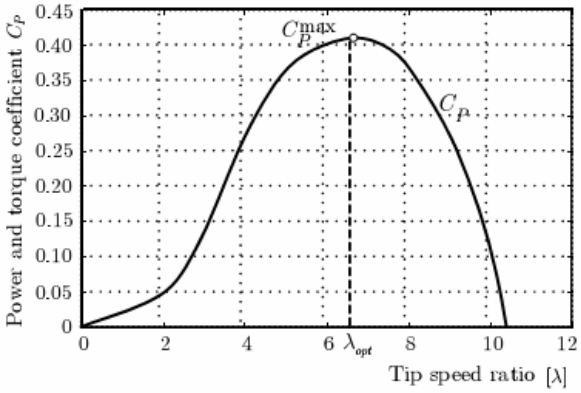

Fig. 2. Power coefficient $C_P(\lambda)$ of real 3 kW wind turbine.

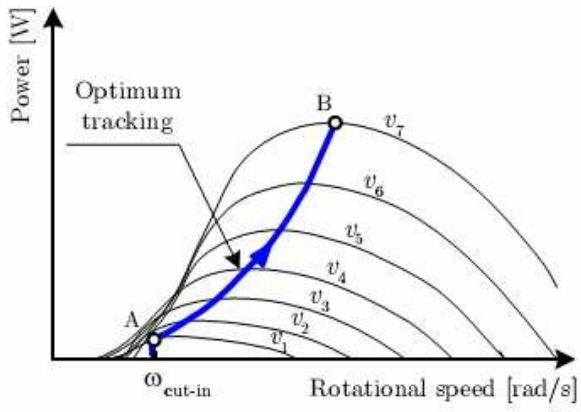

Fig. 3. Power characteristic and optimum power tracking paths.

2.2 Maximum Peak Power Tracking

Figure 4 shows typical characteristics of power and torque versus tip speed ratio of a wind turbine that needs to be controlled. The main purpose of the MPPT controller is to maintain the operating point at $P_m^{\max}$ for any wind speeds in the below rated wind speed region. At any instant of time, the operating point can be at the positive slope of the curve Fig.4 (the left hand side of the $P_m^{\max}$), at zero slope (the point where $P_m^{\max}$ occurs), or at negative slope (the right hand side of the $P_m^{\max}$). If an operating point is in the positive slope region, the controller will move it to the right to get closer to the

maximum. This can be achieved by decreasing load current, which results in an increase in rotational speed. Conversely, if the operating point lies on the right hand side of the peak, the load current has to be increased, resulting in a decrease in the rotational speed.

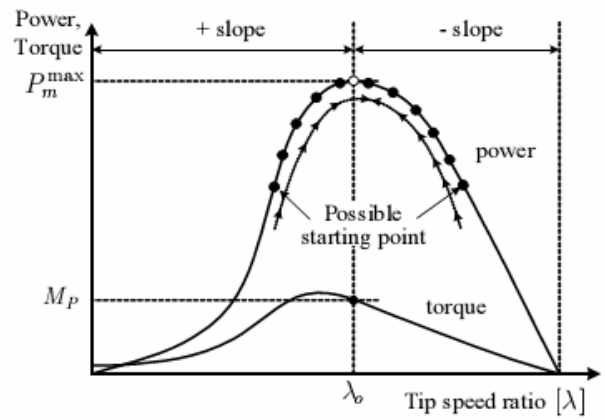

Fig. 4. MPPT process.

2.3 Line Side Converter

The line side converter links the MPPT unit with the grid. Figure 5 shows the three phase line side converter (power unit) that converts AC voltage to DC voltage by a space vector PWM converter. The per phase voltage equation can be written as in (9)-(11). [4-8]

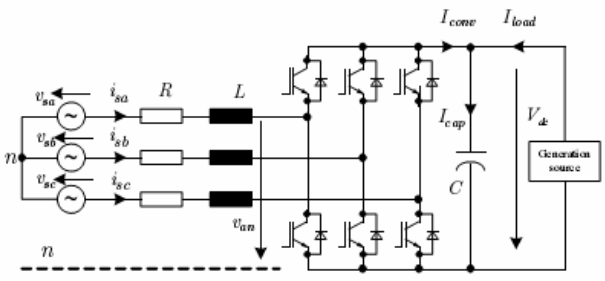

Fig. 5. Line side converter (power unit).

$$v_{sa} = Ri_{sa} + L\frac{di_{sa}}{dt} + v_{an} \tag{9}$$

$$v_{sb} = Ri_{sb} + L\frac{di_{sb}}{dt} + v_{bn} \tag{10}$$

$$v_{sc} = Ri_{sc} + L\frac{di_{sc}}{dt} + v_{cn} \tag{11}$$

Transforming (9)-(11) in three phases in stationary reference frame to two phase synchronous reference frame (*d*-, *q*-axis) gives:

$$v_{sd} = (Ls + R)i_{sd} - \omega Li_{sq} + v_{dn} \tag{12}$$

$$v_{sq} = (Ls + R)i_{sq} + \omega Li_{sd} + v_{qn} \tag{13}$$

For the balance three phase system,

$$v_{sd} = V_m \text{ and } v_{sq} = 0 \tag{14}$$

The converter power, P_{conv}, and current, i_{conv}, can be calculated by (15) and (16) [3].

$$P_{conv} = \frac{3}{2}\left(v_{sd}i_{sd} + v_{sq}i_{sq}\right) \tag{15}$$

$$I_{conv} = \frac{P_{conv}}{V_{dc}^*} = \frac{3}{2}\frac{\left(v_{sd}i_{sd} + v_{sq}i_{sq}\right)}{V_{dc}^*} \tag{16}$$

The capacitor current, I_{cap}, and DC bus voltage, V_{dc}, can be calculated by (17) and (18).

$$I_{cap} = I_{conv} - I_{load} \tag{17}$$

$$V_{dc} = \frac{1}{Cs}\int I_{cap}dt \tag{18}$$

With the transformation of (12)-(18) into s-domain, a block diagram in *d*-, *q*-axis reference frame can be constructed as shown in the right hand side of Fig. 6 (rectifying model). It is clear that there is voltage cross coupling between v_{dn} and v_{qn}. To have independent control of V_{dc}, the coupling voltage should be compensated by a controller [4-5].

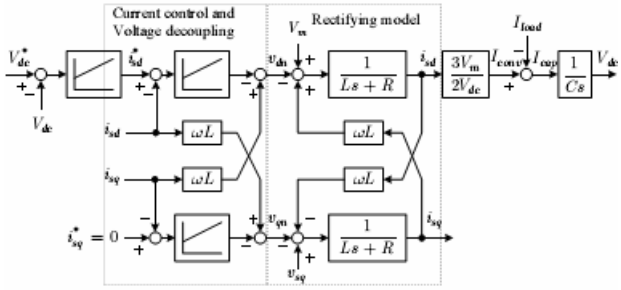

Fig. 6. Line side converter with voltage decoupling control.

3. CONTROL BLOCK DIAGRAM

3.1 MPPT Controller with Grid Connected Wind Turbine

Figure 7 shows the power circuit connection of this system composed of the MPPT controller with the boost converter, the line side converter and the grid. The MPPT controller receives the rotational speed, w, generator voltage, V_g, and current, i_g, to calculate a change of rotational speed to obtain the maximum output power. The MPPT controller increase or decrease the speed by decreasing or increasing the duty cycle of the full-bridge converter. Accordingly, the output voltage will decrease/increase. The voltage will be stepped up by the transformer T_1 and rectified by the full bridge and the capacitor C_1 in order to match the voltage of the line side converter in the next part. If the output voltage is higher than a specified dc bus voltage (550V), the energy will flow to the grid passing through the line side converter (higher voltage and therefore higher energy is flowing to the grid). The energy will stop flowing when the boosted voltage is equal to or less than the specified value.

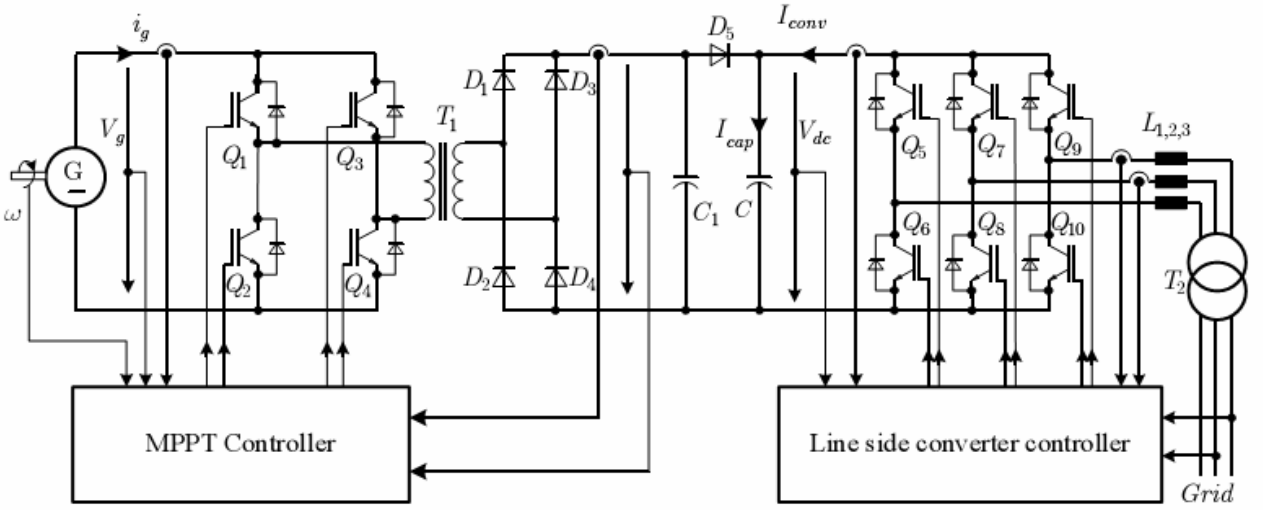

3.2 MPPT Controller

The MPPT controller in the lower left corner of Fig. 7 can be explained in more detail as shown in the block diagram in Fig. 8. The top part of the diagram which is enclosed in the dotted line represents the MPPT controller built from (19) and (20). The MPPT controller receives the generator current, voltage and rotational speed from the plant as inputs and uses them to calculate the slope of the power-speed curve. The rate of change of power is compared with the reference (zero rate of change of power). The error is multiplied by the dc gain, M , to generate the current reference for the PI controller of the plant control system.

The tracking process can be achieved by decreasing load current, which results in an increase in the rotational speed. On the other hand, if the operating point lies at the right hand side of the peak power point, the load current has to be increased, resulting in the decrease in the rotational speed. The step increase or decrease of load current is made with reference to the relative position with $P_m^{\max}$. This tracking methodology is called the perturbation and observation method (P&O). The current reference is calculated from

$$i_{bref}[(k+1)T_s] = i_{bref}[(k)T_s] + M\frac{\Delta p[(k)T_s]}{\Delta\omega_t[(k)T_s]} \qquad (19)$$

The slope of instantaneous power curve is given by

$$slopc = \frac{\Delta p[(k)T_s]}{\Delta\omega_t[(k)T_s]} \qquad (20)$$

The current reference is updated by the MPPT controller at every time step T_s . The above mentioned actions bring the operating point towards $P_m^{\max}$ by step-by-step increasing or decreasing the rotational speed.

3.1 Line Side Converter Controller

In Fig. 6, the voltage cross coupling is compensated by feeding i_{sd} and i_{sq} with gain wL on the left hand side of Fig.6. After the voltage is decoupled, the DC bus voltage is controlled by two loops: current and voltage loops. The current i_{sq} does not affect the bus voltage and therefore it is not used and the value of i_{sq} is set to zero.

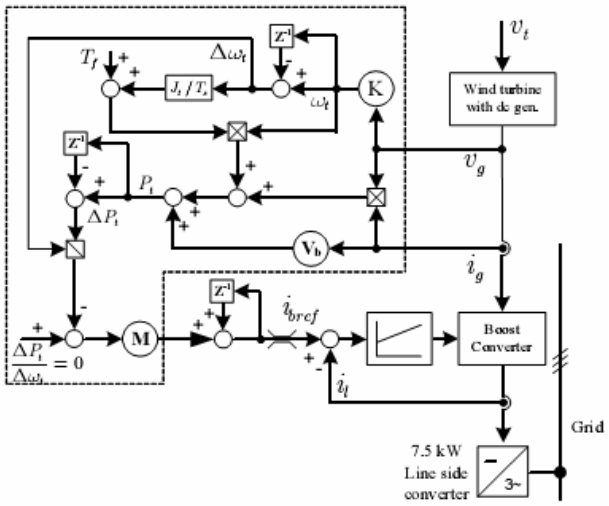

Fig. 8. Block diagram of the MPPT control system with grid connected wind turbine.

The line side converter controller in the lower right corner of Fig. 7 can be explained in more detail as shown in the block diagram of Fig. 9. The controller of the line side converter is controlled in the *d*-, *q*-axis reference frame. The transformation between three phases and the *d*-, *q*-axis requires an angle of phase voltage. A phase locked loop (PLL) to calculate the angle of phase voltage, θ^*, is shown in Fig. 4 [6]. The PLL is composed of voltage transformation, sine and cosine calculation and PI controller. The parameter θ^* in the transformation is obtained by integrating frequency command ω^*. If the frequency is identical to the grid frequency, the voltages v_{sd} and v_{sq} become DC values, depending on the angle θ^*. A PI regulator is used to obtain that value of ω^*, which drives the feedback voltage v_{sq} to the command value v_{sq}^*. The magnitude of the controlled quantity v_{sq} determines the phase difference between the utility

voltages and sin(θ^*) or cos(θ^*). This system sets $v_{sq}^* = 0$.

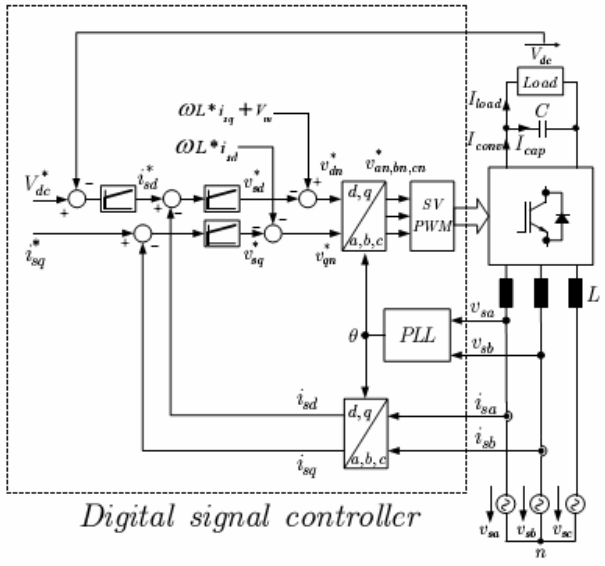

Fig. 9. Line side converter control block diagram.

4 CASE STUDY

Test System

There are two main parts of the test system shown in Fig. 10: 1) a wind turbine simulator [11] on the left hand side of Fig. 10 and 2) a purposed wind turbine controller on the right side of Fig. 10. The data of the wind turbine is provided in appendix. The first part is given in detail in [11] and not repeated here because of limited space. The proposed controller consists of a boost converter connected between a generator line side converter and the grid (a load), voltage and current sensors, a data acquisition unit and a DSC controller. The controller board uses a high performance 16 bits dsPIC30f6010 combining the advantage of a high performance 16-bit microcontroller (MCU) and a high computation speed digital signal processors. Software was implemented in this DSC and performed to link a personal computer via two RS232 ports: one for transferring wind speed data to the DSC board and the other for sending parameters (e.g., P_e, i_g, v_g, w_g) to the computer.

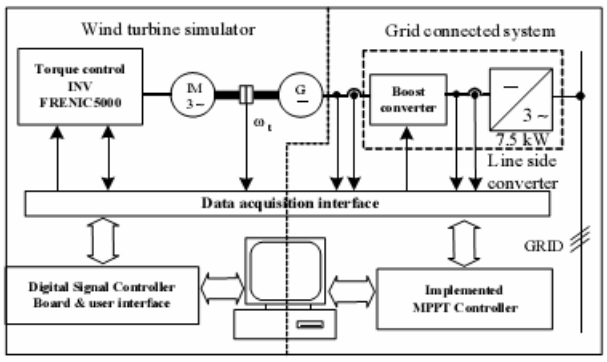

Fig.10. The test system.

4.1 MPPT Control Trajectory with Step Wind Speed

The experiment began by starting up the wind turbine simulator at a wind speed of 4.5m/s to verify the tracking performance of the developed MPPT controller. The controller would try to track the maximum peak power as fast as possible by reducing P_e and thus resulting in an increase in w_t. When an operating point with the maximum power was found (i.e., $dP_t / dw_t = 0$), the controller tried to keep staying at that point.

The objective of this experiment was to track the maximum output power of the turbine. The wind simulator was started at a wind speed of 4m/s , stepped up to 4.5, 5 and 6 m/s respectively and run until steady state. The MPPT controller would capture maximum powers of 260, 420, 600 and 900 W respectively. The power versus rotational speed is shown in Fig. 11 and the output torque versus rotational speed is shown in Fig. 12. It is clearly seen that at the maximum output power, the aerodynamic torque are not maximum. Figure 13 (a) shows the relationship between c_P and time obtained from the experiment. It can be seen from the figure that in this case, the MPPT controller can manage to keep c_P at 0.4 for the four step wind speeds. The power for each wind speed is shown in Figure 13 (b).

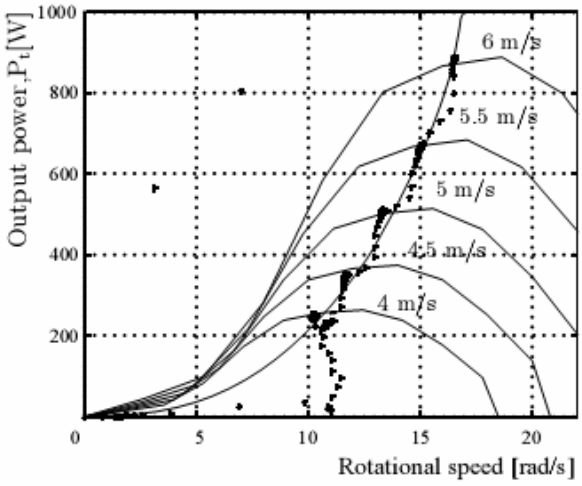

Fig. 11. The control trajectory of MPPT controller in the power versus rotational speed with various wind speed.

MPPT Control Trajectory with Real Wind Speed Data

This experiment used a real wind speed data set obtained from a site in Trung, a province situated in the southern part of Thailand, as the input of the wind turbine simulator. The data are classified as variable wind speed. Figure 14 shows the real wind speed data and the output power controlled by the MPPT controller. Figure 15 plots the control trajectory of the output power versus rotational speed. It is clear that the MPPT controller can track the maximum with the variable wind speed.

Grid Connect Converter

The line side converter is tested with the condition that the power factor of the line side is kept at unity. A

conventional PI controller is implemented. Figure 16 shows the dynamic performance of the line side converter, the DC link voltage and currents i_{sd} and i_{sq} response for step load disturbance rejection. It can be seen that, the line side converter controller decrease i_{sd} to regulate the DC link voltage with low percentage of overshoot.

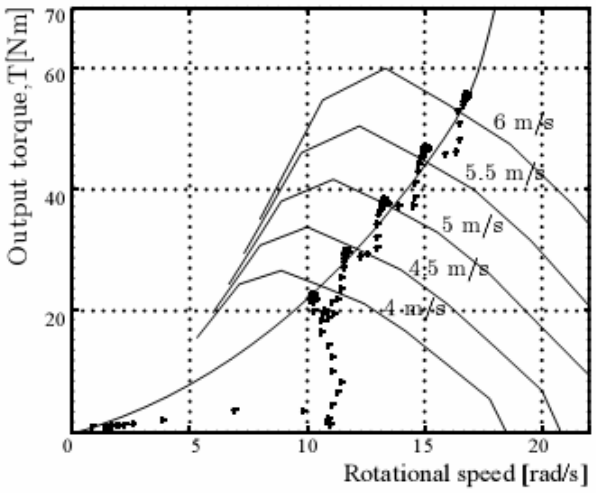

Fig. 12. The control trajectory of MPPT controller in the torque versus rotational speed with various wind speed.

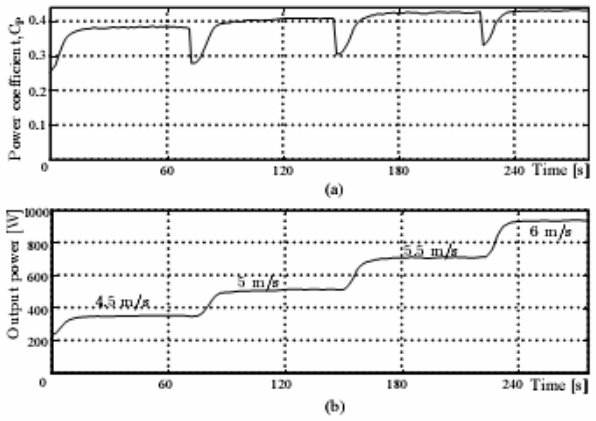

Fig. 13. Output power and power coefficient with time.

Figure 17 shows the phase voltage and phase current of the grid connected line side converter. It can be seen that voltage and current are 180 degree out of phase. Therefore, the power flow from the wind turbine to grid with a phase current near sinusoidal with low harmonic distortion.

CONCLUSION

The control performance of the MPPT controller is verified by the developed 7.5 kW wind turbine simulator. The MPPT controller and line side converter are implemented on a dsPIC 30f6010 digital signal controller board with C language. Experiments are set up for testing the control performance of the MPPT controller and line side converter in inverting modes with grid connection. The experimental results confirm that the system can track the maximum output power with various wind speeds and can regulate the DC bus voltage under nonlinear load generated from the wind turbine with nearly sinusoidal line side current, near-unity power factor and low harmonic distortion. The advantages of the MPPT controller are that it does not require any knowledge of a machine model, and turbine characteristic curves. The developed MPPT controller is useful in case of, for example, dirty blades, varying local air flow effects or blades with non-optimum pitch angles. Although these factors change the characteristics of the wind turbine, they do not affect the proposed control strategy.

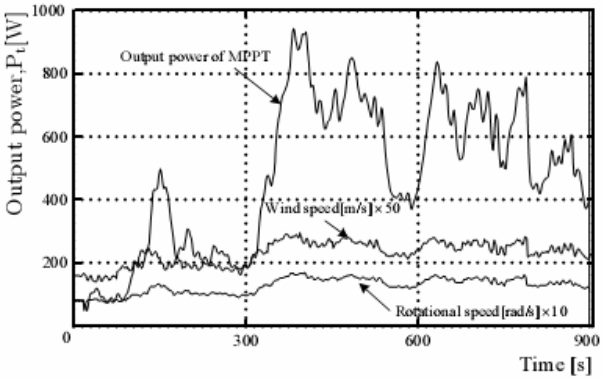

Fig. 14. Real wind speed and the corresponded output power.

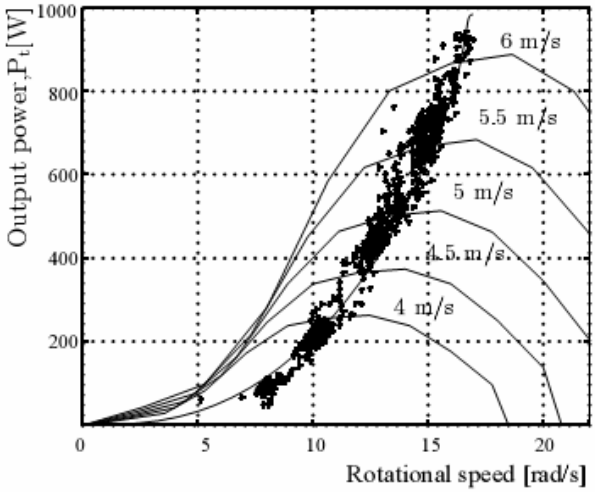

Fig. 15. The control trajectory of MPPT controller in the power versus rotational speed with various wind speed.

ACKNOWLEDGMENT

The authors would like to give a special thank to Department of Alternative Energy Development and Efficiency, Ministry of Energy, Thailand for the wind speed data used in the experiments.

NOMENCLATURE

T_a	wind turbine mechanical torque;
T_c	load torque;
J	turbine moment of inertia;

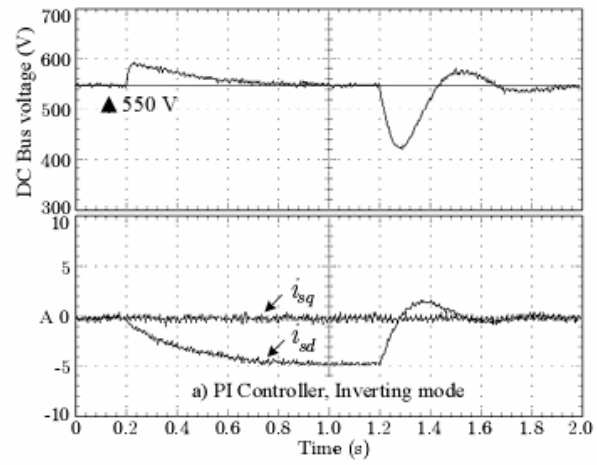

Fig.16. DC bus voltage with step wind speed.

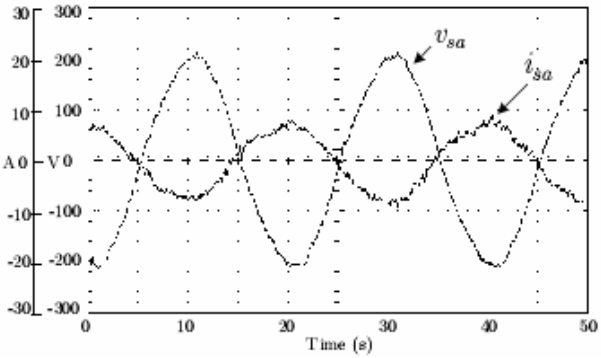

Fig. 17. Line voltage, v_{sa} and current, i_{sa} in inverting mode.

ω	turbine angular speed;
B	friction
P_a	turbine mechanical power;
P_W	wind power
P_{out}	system output power;
P_c	turbine load power;
v	wind speed
A	sweeping area of turbine rotor
C_P	turbine performance coefficient;
λ	tip-speed ratio;
R	maximum radius of the turbine rotor;
η	efficiency of the generator-inverter set
ρ	air density
k_T	Torque constant
v_{sd} , v_{sq}	d- and q-axis voltages
i_{sd} , i_{sq}	d- and q-axis currents
V_{dc}	dc bus voltage
I_{load}	Load current
I_{cap}	Capacitor current
I_{conv}	converter current
P_{conv}	converter power
V_m	Peak voltage
k	constant which depends on the transformation used
R ,	input filter resistance
L_1, L_2, L_3	inductance
$Q_1, Q_2, ..$	IGBT
T_1, T_2	transformer
$D_1, D_2, ..$	diode
V_g	Generator voltage
i_g	Generator current
v_t	Wind speed
V_b	Brush voltage
P_{loss}	losses in the converter
i_{load}	load current connected to the DC link capacitor
$i_{brcf}(k)$	reference current at k
M	step size
T_s	update time

REFERENCES

[1] Neammanee, B., Chatratana, S. 2006. Maximum Peak Power Tracking Control for the new Small Twisted H-Rotor Wind Turbine. In *Proc. of International Conference on Energy for Sustainable Development: Issues and prospect for Asia*, Phuket, Thailand, 1-3 Mar.

[2] Koutroulis E., Kalaitzakis K., Voulgaris N.C. 2001. Development of a Microcontroller-Based, Photo-voltaic Maximum power Point Tracking Control System. *IEEE Trans. Power Electronics*, 16: 46-54.

[3] Huynh, P., Cho, B.H. 1996. Design and analysis of a Microprocessor-Controlled Peak-power-Tracking System. *IEEE Trans. Aerospace and Electronic Systems*, 32(1): 182 – 190.

[4] Sudmee, W., Neammanee, B. 2007. Control and Implementation of Line Side Converter for Doubly Fed Induction Generator of Wind Turbine. *International Conference on Electrical Engineering Electronics, Computer, Telecommunications and Information Technology (ECTI)*, Chiang Rai, Thailand, 9-12 May, 249-252.

[5] Dixon. J.W., Ooi. B.T. 1988. Indirect current control of a unity power factor sinusoidal boost type three-phase rectifier. *IEEE Trans. Industrial Electronic*, 35(4): 508-515.

[6] Rim, C.T., Choi, N.S., Cho G.C., Cho, G.H. 1994. A complete DC and AC Analysis of Three-phase Current PWM Rectifier Using d-q Transformation. *IEEE Trans. Power Electronics*, 9(4): 390-396.

[7] Lee, D.-C. 2000. Advanced nonlinear control of three-phase PWM rectifiers. *IEE Proc. on Electric Power Appl.*, 147(5): 361-366.

[8] Kaura, V., Blasko, V. 1997. Operation of a Phase Locked Loop System under Distorted Utility Condition. *IEEE Trans. Industry Application*, 33(1): 58-63.

[9] Carrasco, J.M., Franquelo, L.G., Bialasiewicz, J.T. Galvan, E., PortilloGuisado, R.C., Prats, M.A.M., Leon. J.I., Moreno-Alfonso, N. 2006. Power-Electronic Systems for Grid Integration of

Renewable Energy Sources: A Survey. *IEEE Trans. Industry Electronics*, 53(4): 1002-1016.

[10] Schulz, D., Fabis, R., Hanitsch, R.E. 2003. A Three Phase Power Electronic Converter for Grid Interration of Distributed Generation. *Power Tech Conference Proceedings*, 23-26 June, Bologna, Italy, 1002-1016.

[11] Neammanee, B., Sirisumrannukul, S., Chatratana, S. 2007. Development of a Wind Turbine Simulator for Wind Generator Testing. *International Energy Journal*, 21-28.

APPENDIX

This is the wind turbine simulator parameters

Wind turbine type	Horizontal
Number of blades	3 blades
Maximum power coefficient	0.40
Optimum tip speed ratio	5
Blade radius	2.25 m
Gear ratio	8
Turbine moment of inertia	11.3

On the Coordinated Control of Multiple HVDC Links: Modal Analysis Approach

Robert Eriksson and Valerijs Knazkins

***Abstract*— *There are several possibilities to improve the small-signal stability in a power system. One adequate option is to make use of available power system components that possess high controllability properties such as, for instance, high voltage direct current (HVDC) systems. This paper presents results from a study aimed at the investigation of small-signal stability enhancement achieved by proper coordinated control of multiple HVDC links. Modal analysis was used as the main tool for the theoretical investigation. The obtained results indicate that the coordinated control of several HVDC links in a power system may assist achieving in an essential increase of damping in the power system. Another important conclusion from the paper is that the possibilities of the coordination of the HVDCs to a certain extent depend on the structure of the grid, which can be investigated by examining the controllable subspace of the linearzied model of the power system.*

***Keywords*— Coordinated control, HVDC, Modal analysis, Power System Stability.**

1. INTRODUCTION

Modern interconnected electric power systems are characterized by large dimensions and high complexity of the structure and the dynamic phenomena associated with the power system operation and control. Power system deregulation that took place in many countries worldwide was one of the driving forces that stimulated a fuller utilization of power systems, which in some cases lead to a reduced stability margin, as the power systems became more stressed. Under these circumstances it becomes quite important to seek new possibilities of enhancement of both transient and small-signal stability of the power systems.

There are several obvious ways of improving power system stability, namely, (*1*) building new transmission lines, (*2*) installing new generation capacities, (*3*) better utilization of the existing equipment in the power system, or (*4*) a combination of the above. This paper is primarily concerned with third option, since compared to the other options it is less costly and can be easily implemented in a real power system. The central idea of the study presented in this paper is the utilization of several HVDC links for small-signal stability enhancement.

The central purpose of conventional HVDC transmission is to transfer a certain amount of electrical power from one node to another and to provide the fast controllability of real power transfer. If the HVDC link is operated in parallel with a critical ac line the load-flow of the ac line can be controlled directly. The presence of an HVDC can assist in improving the stability margin in the power system [1]. In case there are several HVDC links in the system, there is also a possibility of coordinating the HVDC links to enhance the operation of the system [by, for example, altering the load-flow patterns] and to improve the system stability evermore.

The power systems are known to be operated most of the time in the so-called `quasi-steady state'. That is to say, the power systems are always subject to various—often small—disturbances [2]. A change in the loading level or capacitor switching is typical examples of such small disturbances that sometimes give rise to oscillations in the power system. The oscillations are often positively damped and their magnitudes decrease after a while thus the system remains stable.

In case of negative damping of the oscillations the situation is opposite and may result in loss of synchronism unless preventive measures are taken.

2. CASE STUDY

The aim of this paper is to perform modal analysis using coordinated control of two conventional HVDC links in a benchmark power system. This paper also explores the possibilities brought by the controllability and coordination of the HVDC links to enhance the rotor angle stability upset by a disturbance.

In the benchmark power system, as is in all realistic cases, the turbine action is very slow compared to the fast controllability of the HVDC. The theory in this paper is based on small-signal analysis by linearizing the system around the stable or unstable equilibrium point. The modal analysis provides valuable information about the inherent dynamic characteristics of the system. By controlling the current through the HVDCs and using state feedback it is possible to move the eigenvalues to pre-specified locations in the complex plane and thereby increase the damping.

3. TEST POWER SYSTEM

The system in this case study consists of three generators connected to nodes A, B, and C. The HVDC links are

R. Eriksson (corresponding author) is with the Division of Electric Power Systems at Royal Institute of Technology, (KTH), Teknikringen 33, 100 44 Stockholm, Sweden. Email: robert.eriksson@ee.kth.se.

V. Knazkins is with the Division of Electric Power Systems at Royal Institute of Technology, (KTH), Teknikringen 33, 100 44 Stockholm, Sweden. Email: valerijs.knazkins@ee.kth.se.

connected between nodes A and C and between B and C. The power production is large in node A and the load center is assumed to be in node C, i.e., there is a significant power flow from nodes A to C. The power can go either through the ac lines or through the HVDC links. An overview of the test power systems is shown in Fig. 1.

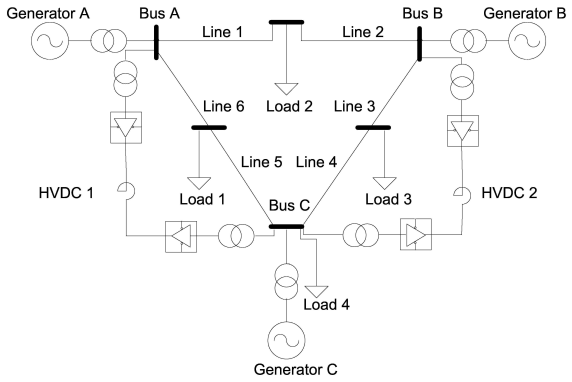

Fig. 1. Test Power system.

4. SYSTEM MODEL

The HVDC link is of a classical type, which implies that it consumes reactive power and that the active power can be controlled. The HVDC link consists of an ideal rectifier, inverter, and series reactor which models the dc-line and creates a smooth dc current. The power through the HVDC is controlled by controlling the firing angle, α. The firing angle is controlled by a basic PI-controller and the input is the set point current. The generators are modelled by the one axis model, described by equations (1)-(3) [3], thus three states per generator are used. The dynamics of the HVDC [4] are described in equations (4)-(16), where the subscripts "*r*" and "*i*" refer to rectifier and inverter, respectively.

$$\dot{\delta} = \omega \tag{1}$$

$$\dot{\omega} = \frac{1}{M}\left(P_m - P_e - D\omega\right) \tag{2}$$

$$\dot{E}'_q = \left(E_f - \frac{x_d}{x'_d}E'_q + \frac{x_d - x'_d}{x'_d}V\cos(\delta-\theta)\right) \tag{3}$$

where

- δ is the rotor angle
- ω is the rotor synchronous speed
- $E'_q\angle\delta$, $V\angle\theta$ are the voltage phasors at the internal and terminal buses
- T'_{do} is the d-axis transient open-circuit time constant
- P_m is the mechanical power applied to the generator shaft
- D is the generator's shaft damping constant
- M is the machine inertia
- x_d is the d-axis synchronous reactance
- x'_d is the d-axis transient reactance
- E_f is the constant generator field voltage

$$\dot{I}_d = \frac{1}{L_d}(V_{d_r} - V_{d_i}) - \frac{R_d}{L_d}I_d \tag{4}$$

$$\dot{x}_r = K_I(I_{d_{setp}} - I_d) \tag{5}$$

$$\dot{x}_i = K_I(I_d - I_{d_{setp}}) \tag{6}$$

$$\cos(\alpha_r) = x_r + K_P(I_{d_{setp}} - I_d) \tag{7}$$

$$V_{d_r} = \frac{3\sqrt{2}}{\pi}V_{r_{pu}}\cos(\alpha_r) - \frac{3}{\pi}X_{C_r}I_d \tag{8}$$

$$S_r = -\frac{3\sqrt{2}}{\pi}\frac{V_{b_{dc}}I_{b_{dc}}}{S_{b_{dc}}}V_{r_{pu}}I_d \tag{9}$$

$$P_r = -\frac{V_{b_{dc}}I_{b_{dc}}}{S_{b_{dc}}}V_{d_r}I_d \tag{10}$$

$$Q_r = -\sqrt{S_r^2 - P_r^2} \tag{11}$$

$$\cos(\gamma_i) = x_i + K_P(I_d - I_{d_{setp}}) \tag{12}$$

$$V_{d_i} = \frac{3\sqrt{2}}{\pi}V_{i_{pu}}\cos(\gamma_i) - \frac{3}{\pi}X_{C_i}I_d \tag{13}$$

$$S_i = \frac{3\sqrt{2}}{\pi}\frac{V_{b_{dc}}I_{b_{dc}}}{S_{b_{dc}}}V_{i_{pu}}I_d \tag{14}$$

$$P_i = \frac{V_{b_{dc}}I_{b_{dc}}}{S_{b_{dc}}}V_{d_i}I_d \tag{15}$$

$$Q_i = -\sqrt{S_i^2 - P_i^2} \tag{16}$$

where

- V_{d_r}, V_{d_i} are the per unit dc terminal voltages at the rectifier and inverter
- $V_{b_{dc}}, I_{b_{dc}}, S_{b_{dc}}$ are the base quantities at the dc side for the voltage, current and power, respectively
- X_{c_r}, X_{c_i} are the unit commutation reactances
- R_d, L_d are the per unit dc line parameters
- $V_{r_{pu}}, V_{i_{pu}}$ are the per unit ac bus voltages
- $I_{d_{setp}}$ is the current set point through the HVDC

5. MODAL ANALYSIS

To study the power system small-signal stability problem, an appropriate model for the machines, loads

and HVDC dynamics is required. The behavior of a power can be described by a set of first order nonlinear ordinary differential equations and a set of nonlinear algebraic equations [3].

$$\dot{x} = f(x, y, u) \tag{17}$$

$$0 = g(x, y, u) \tag{18}$$

where

$x = (\delta^T \omega^T E_q'^T I_d^T x_r^T x_i^T)^T$ is the vector containing the state variables, $y = (\theta^T V^T)^T$ is the vector designating algebraic variables, and finally $u = I_{d_{setp}}$ the defined as the vector of control variables.

In the small signal stability analysis, the equations (17) and (18) are linearized at an equilibrium point and the higher order terms are neglected. The linearization gives the structure as follows:

$$\begin{cases} \Delta\dot{x} = f_x \Delta x + f_y \Delta y + f_u \Delta u \\ 0 = g_x \Delta x + g_y \Delta y + g_u \Delta u \end{cases} \Rightarrow \tag{19}$$

$$\begin{aligned} \Delta\dot{x} &= (f_x - f_y g_y^{-1} g_x)\Delta x + (f_u - f_y g_y^{-1} g_u)\Delta u \\ &= J_x \Delta x + J_u \Delta u. \end{aligned} \tag{20}$$

The prefix Δ means a small increment in corresponding variables. The matrices in equation (19) and (20) can be found in appendix.

The Lyapunov's first stability method is the fundamental analytical basis for power system small-signal stability assessment. It is based on eigenvalue analysis and provides valuable information of the behavior of the system, i.e. the time domain characteristics of a system mode. It is usual to associate each eigenvalue λ_i with a mode of the system. Real eigenvalues represent non-oscillatory modes, where a negative one corresponds to decaying mode, while a positive one relates to aperiodic instability. Complex eigenvalues are associated with system oscillatory modes, the pair of complex eigenvalues with negative real parts indicate a decreasing oscillatory behavior, and those with positive real parts result in an increasing oscillatory behavior. The damping of the i:th mode is defined as follows:

$$\xi_i = \frac{-\sigma_i}{\sqrt{\sigma_i^2 + \omega_i^2}} \tag{21}$$

where

$$\sigma_i = \Re e(\lambda_i)$$

$$\omega_i = \Im m(\lambda_i)$$

By controlling the HVDCs and thereby controlling the modes it is thereby possible to change the behavior of the system. The controllable subspace provides information how the eigenvalues can be moved i.e. how the system can be controlled. The Kalman decomposition transforms the state space model into controllable, uncontrollable, observable and unobservable subspaces [5],[6]. Where the controllable and uncontrollable subspaces are of interest, since they provide information about how the eigenvalues can be moved. The matrices J_x and J_y span the controllability matrix and the image of the corresponding map is the controllable space. The proposed method can thereby be used for practical and large scale power systems. By following the above described procedure the controllability gramian provides the information how the poles can be moved, i.e., how the damping in the system can be increased.

The eigenvalues can nor be moved arbitrary in the controllable subspace due to limitations in the current through the HVDCs.

6. SIMULATION STUDY

In the test power system the eigenvalues of J_x in equation (20) are determined. It results in two oscillatory modes which are referring to the system model. The eigenvalues can be found in Table 1.

The damping in the system is about 5%. By using state feedback it is possible to increase the damping. The control is performed as showed in Fig. 2. This is full state feedback which means all states are used in the feedback, if not all the states are available, it possible to perform state estimation. The unavailable signals can be estimated by an observer, but this situation is left outside of the scope of this paper.

Table 1. Eigenvalues of the linearized system

$\lambda_{\text{no feedback}}$	$\xi_{\text{no feedback}}$	$\lambda_{\text{feedback}}$	ξ_{feedback}
-0.552 + 9.780i	0.0564	-2.887	1
-0.552 - 9.780i	0.0564	-2.887	1
-1.179 + 13.258i	0.0886	-3.464	1
-1.179 - 13.258i	0.0886	-3.464	1
-0.102	1	-2	1
-0.496	1	-2.25	1
-0.716	1	-2.5	1
-0.849	1	-2.75	1
-1.138	1	-3	1
-1.138	1	-3.25	1
-2.373	1	-3.5	1
-2.373	1	-3.75	1
0	-	-4	1
0	-	0	-
0	-	0	-

The output may be chosen arbitrarily from the states or a linear combination of the states. However, in this paper generator A is taken as the reference and the outputs are the deviation in speed of generator B and generator C, i.e. *output one* = ω_C-ω_A and *output two* = ω_B-ω_A. The output is related to the states by a matrix which is linearly combining the state to the output. This is shown in Fig. 2 and the relating matrix is denoted as J_y.

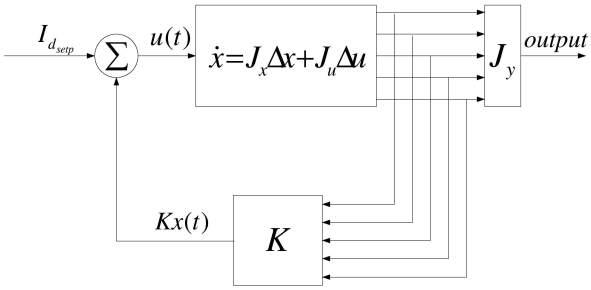

Fig. 2. State feedback.

In the case study in this paper all the eigenvalues can be moved arbitrarily. One possibility is to increase the damping or remove the oscillatory modes completely. In the test power system the closed loop system has the eigenvalues given in Table 1.

Two disturbances are applied to the system, the disturbances are due to load changes. Case one is due to a decrease of load 1 and increase of load 3. Case two is due to decrease of load 2 and increase of load 3. In both the cases the increase and the decrease are equal, which is done to preserve the equilibrium point. Fig. 3 and Fig. 4 show the output signals when disturbance one is applied. It is obvious that inspection of the figures reveals that the system behaves more nicely when using the state feedback and the oscillatory behavior should be totally eliminated, since all ω_i.=0 Fig. 5 and **Fig. 6** show the system behavior under disturbance two, and also in this case, the response is better in the controlled system compared to the uncontrolled.

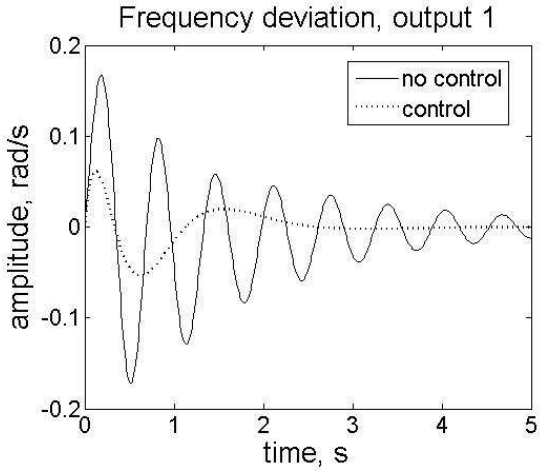

Fig. 3. Disturbance one i.e. increase of load 3 and decrease of load 1. Output one i.e. speed difference of generator C and A.

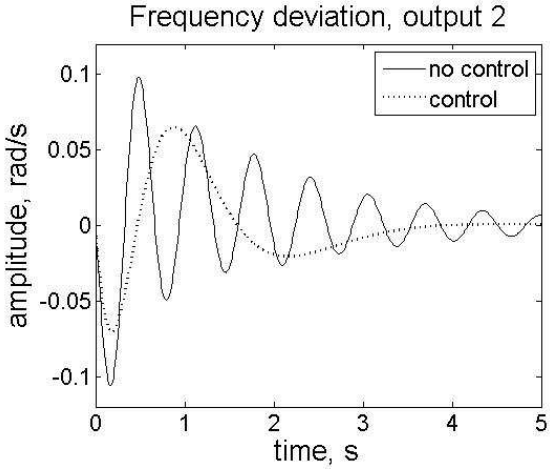

Fig. 4. Disturbance one i.e. increase of load 3 and decrease of load 1. Output two i.e. speed difference of generator B and A.

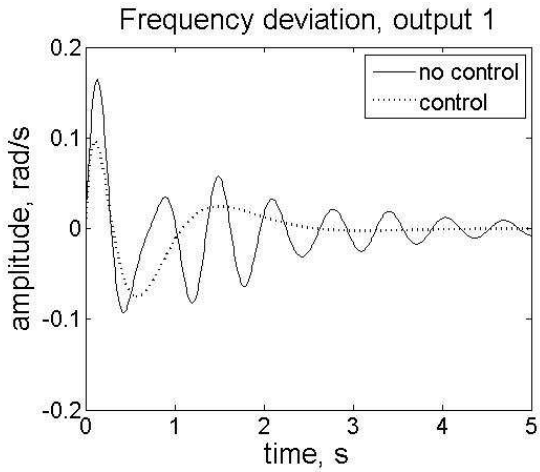

Fig. 5. Disturbance two i.e. increase of load 3 and decrease of load 2. Output one i.e. speed difference of generator C and A.

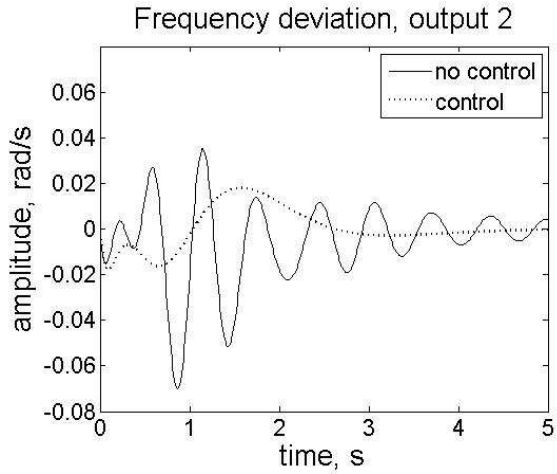

Fig. 6. Disturbance two i.e. increase of load 3 and decrease of load 2. Output two i.e. speed difference of generator B and A.

7. CONCLUSIONS

This paper presents modal analysis of a power system

with several HVDC links and investigates the possibility to increase the damping in the system by changing the modes in the system. The obtained results strongly indicate that essential enhancement of small-signal stability can be achieved by proper coordination of the control of the HVDC links.

The paper also describes the ideas about the controllability of the modes, which are depending of the structure of the grid and may be determined as the controllable subspace.

REFERENCES

[1] Adapa, R. 2002. Facts system studies. *IEEE Power Engineering Review*.

[2] Handschin, E. Et al. 1972 *Real-Time Control of Electric Power Systems.* Elsevier Verlag Amsterdam, 1972.

[3] Kundur, P. 1993. *Power System Stability and Control*. McGraw-Hill Inc.

[4] Canizares, C.A. 1991. *Voltage Collapse and Transient Energy Function Analysis of AC/DC Systems*. PhD thesis, University of Wisconsin-Madison.

[5] Sontag, E.D. 1998. *Mathematical Control Theory: Deterministic Finite Dimensional Systems*. Springer.

[6] Sigurd Skogestad I.P. 2001. *Multivariable Feedback Control, Analysis and Design*. Wiley.

APPENDIX

In the following section the Jacobian matrices of the linearized system are given.

The following is given: Let N be the number of network buses, and n_g be the number of generators. Also let $n_x = 3(n_g + n_{HVDC})$ be the number all state variables, where n_{HVDC} is the number of HVDC-links. And finally $n_y = 2N$ be the number of all system algebraic variables. Then the Jacobian matrices f_x, f_y, f_u, g_x, g_y and g_u have the structure as follows:

$$f_x = \frac{\partial f}{\partial x} = \begin{pmatrix} \mathbf{0} & \mathbf{f^x_{1,2}} & \mathbf{0} & \mathbf{0} & \mathbf{0} & \mathbf{0} \\ \mathbf{f^x_{2,1}} & \mathbf{f^x_{2,2}} & \mathbf{f^x_{2,3}} & \mathbf{0} & \mathbf{0} & \mathbf{0} \\ \mathbf{f^x_{3,1}} & \mathbf{0} & \mathbf{f^x_{3,3}} & \mathbf{0} & \mathbf{0} & \mathbf{0} \\ \mathbf{0} & \mathbf{0} & \mathbf{0} & \mathbf{f^x_{4,4}} & \mathbf{f^x_{4,5}} & \mathbf{f^x_{4,6}} \\ \mathbf{0} & \mathbf{0} & \mathbf{0} & \mathbf{f^x_{5,4}} & \mathbf{0} & \mathbf{0} \\ \mathbf{0} & \mathbf{0} & \mathbf{0} & \mathbf{f^x_{6,4}} & \mathbf{0} & \mathbf{0} \end{pmatrix}$$

which is of order $n_x \times n_x$
for $k = 1 \ldots n_g$ and for $m = 1 \ldots n_{HVDC}$

$$f^x_{1,2}(k,k) = 1$$

$$f^x_{2,1}(k,k) = -\frac{1}{M_k}\frac{E'_{qk}V_k}{x'_{dk}}\cos(\delta_k - \theta_k)$$

$$f^x_{2,2}(k,k) = -\frac{D}{M_k}$$

$$f^x_{2,3}(k,k) = -\frac{1}{M_k}\frac{V_k}{x'_{dk}}\sin(\delta_k - \theta_k)$$

$$f^x_{3,1}(k,k) = -\frac{x_{dk} - x'_{dk}}{T'_{dk}x'_{dk}}V_k\sin(\delta_k - \theta_k)$$

$$f^x_{3,3}(k,k) = -\frac{x_{dk}}{T'_{dk}x'_{dk}}$$

$$f^x_{4,4}(m,m) = -\frac{3\sqrt{2}K_p}{L_d\pi}(V_{i_{pu}} + V_{r_{pu}}) + \frac{3}{\pi}(X_{c_i} - X_{c_r}) - \frac{R_d}{L_d}$$

$$f^x_{4,4}(m,m) = -\frac{3\sqrt{2}K_p}{L_d\pi}(V_{i_{pu}} + V_{r_{pu}}) + \frac{3}{\pi}(X_{c_i} - X_{c_r}) - \frac{R_d}{L_d}$$

$$f^x_{4,5}(m,m) = \frac{3\sqrt{2}V_{r_{pu}}}{\pi L_d}$$

$$f^x_{4,6}(m,m) = -\frac{3\sqrt{2}V_{i_{pu}}}{\pi L_d}$$

$$f^x_{5,4}(m,m) = -K_I$$

$$f^x_{6,4}(m,m) = K_I$$

$$f_y = \frac{\partial f}{\partial y} = \begin{pmatrix} \mathbf{0} & \mathbf{0} \\ \mathbf{f^y_{2,1}} & \mathbf{f^y_{2,2}} \\ \mathbf{f^y_{3,1}} & \mathbf{f^y_{3,2}} \\ \mathbf{0} & \mathbf{0} \\ \mathbf{0} & \mathbf{0} \\ \mathbf{0} & \mathbf{0} \end{pmatrix}$$

which is of order $n_x \times n_y$
for $k = 1 \ldots n_g$

$$f^y_{2,1}(k,k) = \frac{E'_{qk}V_k}{M_k x'_{dk}}\cos(\delta_k - \theta_k)$$

$$f^y_{2,2}(k,k) = -\frac{E'_{qk}}{M_k x'_{dk}}\sin(\delta_k - \theta_k)$$

$$f^y_{3,1}(k,k) = \frac{x_{dk} - x'_{dk}}{x'_{dk}T_{dk}}V_k\sin(\delta_k - \theta_k)$$

$$f^y_{3,2}(k,k) = \frac{x_{dk} - x'_{dk}}{x'_{dk}T_{dk}}\cos(\delta_k - \theta_k)$$

$$f_u = \frac{\partial f}{\partial u} = \begin{pmatrix} \mathbf{0} & \mathbf{0} & \mathbf{0} & \mathbf{f^u_{4,1}} & \mathbf{f^u_{5,1}} & \mathbf{f^u_{6,1}} \end{pmatrix}$$

which is of order $n_{HVDC} \times n_x$
for $m = 1 \ldots n_{HVDC}$

$$f^u_{4,1}(m,m) = \frac{3\sqrt{2}}{\pi L_d}K_P(V_{r_{pu}} + V_{i_{pu}})$$

$$f^u_{5,1}(m,m) = K_I$$

$$f^u_{6,1}(m,m) = -K_I$$

$$g_x = \frac{\partial g}{\partial x} = \begin{pmatrix} \mathbf{g^x_{1,1}} & \mathbf{0} & \mathbf{g^x_{1,3}} & \mathbf{g^x_{1,4}} & \mathbf{g^x_{1,5}} & \mathbf{g^x_{1,6}} \\ \mathbf{g^x_{2,1}} & \mathbf{0} & \mathbf{g^x_{2,3}} & \mathbf{g^x_{2,4}} & \mathbf{g^x_{2,5}} & \mathbf{g^x_{2,6}} \end{pmatrix}$$

which is of order $n_y \times n_x$
for $k = 1 \ldots n_g$ and $m = 1 \ldots n_{HVDC}$

$$g^x_{1,1}(k,k) = -\frac{E_{qk}V_k}{x'_{dk}}\cos(\theta_k - \delta_k)$$

$$g^x_{1,3}(k,k) = \frac{V_k}{x'_{dk}}\sin(\theta_k - \delta_k)$$

$$g^x_{1,4}(k,m) = \begin{cases} -\frac{V_{bcd}I_{bdc}}{S_b}\left(\frac{3\sqrt{2}}{\pi}V_k(x_r - K_P I_{d_m}) + \frac{6}{\pi}X_{cr}I_{d_m}\right) & * \\ \frac{V_{bcd}I_{bdc}}{S_b}\left(\frac{3\sqrt{2}}{\pi}V_k(x_i + K_P I_{d_m}) + \frac{6}{\pi}X_{ci}I_{d_m}\right) & ** \\ 0 & *** \end{cases}$$

$$g^x_{1,5}(k,m) = \begin{cases} -\frac{V_{bcd}I_{bdc}}{S_b}\frac{3\sqrt{2}}{\pi}V_k I_{d_m} & * \\ 0 & *** \end{cases}$$

$$g^x_{1,6}(k,m) = \begin{cases} \frac{V_{bcd}I_{bdc}}{S_b}\frac{3\sqrt{2}}{\pi}V_k I_{d_m} & ** \\ 0 & *** \end{cases}$$

$$g^x_{2,1}(k,k) = -\frac{E_{qk}V_k}{x'_{dk}}\sin(\theta_k - \delta_k)$$

$$g^x_{2,3}(k,k) = -\frac{V_k}{x'_{dk}}\cos(\theta_k - \delta_k)$$

$$g^x_{2,4}(k,m) = \begin{cases} -C\frac{V_{bcd}I_{bdc}}{S_b}\left(\frac{3\sqrt{2}}{\pi}V_k(x_r - K_P I_{d_m} + \frac{6}{\pi}X_{cr}I_{d_m}\right) & * \\ -C\frac{V_{bcd}I_{bdc}}{S_b}\left(\frac{3\sqrt{2}}{\pi}V_k(x_i + K_P I_{d_m} + \frac{6}{\pi}X_{ci}I_{d_m}\right) & ** \\ 0 & *** \end{cases}$$

$$g^x_{2,5}(k,m) = Cg^x_{1,5}(k,m)$$

$$g^x_{2,6}(k,m) = -Cg^x_{1,6}(k,m)$$

Optimal Placement of Sectionalizing Switches in Radial Distribution Systems by a Genetic Algorithm

K. Klinieam and S. Sirisumrannukul

Abstract*— *Proper installation of sectionalizing switches in a distribution system can improve system reliability. Subjective placement of sectionalizing switches could lead to underinvestment which, although less reliable, can produce unacceptable load point failures or to overinvestment which, although more reliable, is uneconomic. Therefore, placement of sectionalizing switches should be judiciously determined to provide the balance between the utility's cost and the customers' outage cost. This problem falls into a class of combinatorial optimization which can be efficiently solved by a genetic algorithm. The genetic algorithm is used to search for the number of switches and their locations. Reliability cost/worth analysis is then performed to calculate the customer's outage cost. The methodology is illustrated by a subdistribution network of Provincial Electricity Authority (PEA) of Thailand, which consists of 2 primary feeders and 26 load points.

***Keywords*— Distribution system reliability, Genetic algorithm, Sectionalizing switches, Service restoration.**

1. INTRODUCTION

Reliability in a distribution system, which transfers electrical energy from transmission systems to end-user customers, can be improved by the installation of sectionalizing switches. A sectionalizing switch is a device that isolates a faulted part from the system so that the healthy part can still be electrically supplied and the interruption duration is minimized. Switch placement plays an important role in automated distribution network, where the sectionalizing switches can be remotely activated.

Utilities normally employ past experience, customer data, and other consideration for the appropriate number of switches and their locations. Subjective placement of sectionalizing switches would, however, lead to underinvestment and therefore low reliability for the customers. On the other hand, although high reliability, it would lead to uneconomic owing to the utility's increased investment for the installation costs of the switches, which are quite significant as indicated by [1]. Therefore, the evaluation of the costs associated with different placements and the corresponding reliability worth associated with the differences should be judiciously determined.

The solution to the problem presented in this paper is based on a genetic algorithm and reliability cost/worth analysis. Genetic algorithms are stochastic optimization techniques that have a large number of applications, including power system areas, for example optimal reconfiguration distribution networks, optimal capacitor placement in distribution system and optimal power flow. With the genetic algorithm and reliability cost/worth analysis, the optimal placement of sectionalizing devices can be obtained providing the lowest total cost that is the sum of investment cost, maintenance cost and customer outage cost. The methodology is illustrated by a subdistribution network of Provincial Electricity Authority (PEA), which consists of 2 primary feeders and 26 load points.

2. GENETIC ALGORITHM

The genetic algorithm (GA) is a stochastic search technique based on the principles of genetics and natural selection [2]. The GA operates on populations that consist of a number of individuals. The initial population is randomly generated. Each individual is then evaluated to obtain a measure of its fitness in terms of the objective function to be optimized. The algorithm allows a population composed of many individuals to evolve by two basic operators crossover and mutation. The crossover operator creates new individual by combining substrings from the parent individuals. The mutation operator creates a new individual by changing randomly selected bits in its coding. The genetic algorithm employed in this paper is based on the following ten steps [3].

Step 1: Generate population 1 and population 2 which satisfy the constraints of a problem.

Step 2: Evaluate the fitness of each individual in population 2 to find the best fitness of population 2. The fitness is calculated from the objective function.

Step 3: Create a new population 3 from the crossover operator between population 1 and the best fitness individual of population 2. If it turns out that the fitness of an individual in population 3 is better than the best fitness individual in population 2, then that individual in population

K. Klinieam (corresponding author) is with Faculty of Technical Education, King Mongkut's University of Technology North Bangkok (KMUTNB), Bangkok, Thailand. Phone 66-2-9132500 ext.3313; Fax: 66-2-5878255; E-mail: kanokwank@kmutnb.ac.th.

S. Sirisumrannukul is with Faculty of Engineering, King Mongkut's University of Technology North Bangkok (KMUTNB), Bangkok, Thailand. E-mail: spss@kmutnb.ac.th.

3 replaces the best fitness individual. Otherwise, the individual replaces its parent in population 1 with a probability of replacement.

Step 4: Select and keep the best fitness from population 2.

Step 5: Bring population 1 to the crossover and mutation process.

Step 6: This is the same as step 3 except that instead of using the best fitness individual in population 2, a randomly selected individual from population 2 is brought to crossover with some probability.

Step 7: Select and keep the best fitness from population 2.

Step 8: Compare the best fitness individual from step 4 with that of step 7.

Step 9: Update the best fitness individual of population 2 in step 3 with the one obtained from step 8.

Step 10: Repeat step 3 through step 7 until the maximum generation has been reached.

3. RELIABILITY COST/WORTH IN DISTRIBUTION SYSTEMS

A distribution circuit normally uses primary or main feeders and lateral distributions. A primary feeder originates from a substation and passes through major load centers. The lateral distributors connect the individual load points to the main feeder with distribution transformers at their ends. Many distribution systems used in practice have a single-circuit main feeder and defined as radial distribution system. Radial distribution systems are widely used because of their simple design and generally low cost.

A radial distribution system consists of series components (e.g., lines, cables, transformers) to load points. This configuration requires that all components between a load point and the supply point operate and therefore poor reliability can be expected because the failure of any single component causes the load points disconnected. However, many distribution systems have normally open points that can be switched to meshed systems in the event of a system failure [4]. In addition, load point reliability can be improved by installing sectionalizing switches that can remove the faulted part from the remaining healthy system.

Reliability cost is quantified in forms of investment incurred by installation of sectionalizing switches, whereas reliability worth is quantified in forms of customer outage costs served as input data for cost implications and worth assessments of system planning and operational decisions. The customer outage costs are calculated from reliability indices of the load points and customer damage functions. The customer damage function utilized in this paper is shown in Figure 1 [5].

The basic distribution system reliability indices are average failure rate l , average outage duration r , and annual outage duration U. With the three load point indices and load model at load points, system average interruption frequency index (SAIFI), system average interruption duration index (SAIDI), expected energy not supplied (ENS), and expected outage cost (ECOST) can be calculated. These four reliability indices are calculated from

$$SAIFI = \sum_{j=1}^{nj}\sum_{k=1}^{nk} \lambda_j P_k \Big/ \sum_{l=1}^{nl} P_l \tag{1}$$

$$SAIDI = \sum_{j=1}^{nj}\sum_{k=1}^{nk} \lambda_j r_j P_k \Big/ \sum_{l=1}^{nl} P_l \tag{2}$$

$$ENS = \sum_{i=1}^{ni}\sum_{j=1}^{nj}\sum_{k=1}^{nk} L_{ik} r_j \lambda_j \tag{3}$$

$$ECOST = \sum_{i=1}^{ni}\sum_{j=1}^{nj}\sum_{k=1}^{nk} L_{ik} C_{jk}(r_j) \lambda_j \tag{4}$$

where

ni = number of load steps

nk = number of load points that are isolated due to a contingency j

nj = number of outage events

nl = total number of load points

L_{ik} = load at load point k for the i th step of load duration curve at load point k

r_j = average outage time of contingency j

λ_j = failure rate of contingency j

P_k = number of customers connected to a load point k

$C_{jk}(r_j)$ = outage cost (\$/kW) of customer class k due to outage j with an outage duration of r_j

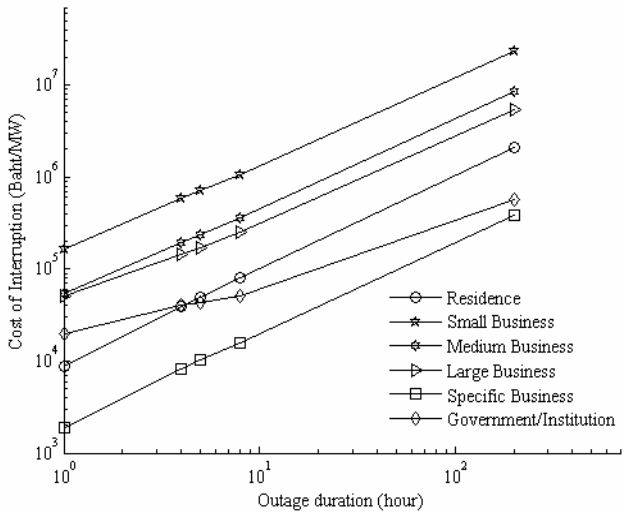

Fig. 1. Customer Damage Function.

4. PROBLEM FORMULATION

The objective function of the problem of sectionalizing switch placement is to select the number of switches and their locations such that the sum of the installation cost maintenance cost and ECOST is minimized subject to

system constraints. The system constraints are voltage and line current limits. The objective function is mathematically expressed by (5). The first two costs of (5) depend on the number of sectionalizing switches whereas the last cost is calculated from (4).

$$\text{Minimize} \sum_{n=1}^{ns} \text{Installation cost} + \sum_{n=1}^{ns} \text{Maintenace cost} + ECOST \quad (5)$$

subject to

$$V_i^{\min} \le V_i \le V_i^{\max}$$

$$I_l \le I_l^{\max}$$

where

ns	=	number of sectionalizing switches
V_i	=	voltage at i th node
I_l	=	current of feeder section l
V_i^{min}	=	minimun voltage at i th node
V_i^{max}	=	maximun voltage at i th node
I_l^{max}	=	rated current of feeder section l

5. DISTRIBUTION POWER IN RADIAL SYSTEM

Load flow solution in a radically operated distribution network can be efficiently solved by the formation of a constant spare upper triangle matrix to determine the bus voltages. This method requires initial voltages, system configuration, and a branch-to-node matrix. The voltages at all nodes are calculated by iterative process without matrix inversion. This method is efficient in terms of speed, convergence and computer storage requirement. The algorithm is described as follows [7].

Step 1: Consider the network topology description, network data, and load data.

Step 2: Form matrix $[C]$ from branch-to-node of the branch currents from topology description of the given system.

Step 3: Assume voltages at all nodes are equal to the source node or initialize all nodes with previously calculate voltage

Step 4: Determine the load current at all nodes by

$$J_i = \frac{P_i - jQ_i}{V_i^*} + \frac{V_i}{Z_i} + Y_i V_i + I_{Li} \qquad i = 1,2,...,nb$$

where

nb	=	number of node (including source node)
n	=	$nb - 1$
b	=	number of branches
V_o	=	source node voltage
J_i	=	load current at i th node
V_i	=	voltage at i th node
P_i, Q_i	=	real and reactive loads at i th node, respectively
Z_i	=	load at i th node modeled by a constant impedance
Y_i	=	load at i th node modeled by a constant admittance
I_{Li}	=	load at i th node modeled by a constant current
$[i_b]$	=	vector of branch currents of order $(b \times 1)$
$[v_b]$	=	vector of branch voltage of order $(b \times 1)$
$[J_L]$	=	vector of load current at all nodes of order $(n \times 1)$
$[C]$	=	branch-to-node matrix of order $(b \times n)$
$[z]$	=	primitive impedance matrix of order $(b \times b)$

Step 5: Determine the branch currents of all branches by $[i_b] = [C][J_L]$

Step 6: Determine the branch voltages of all branches by $[v_b] = [z][i_b]$

Step 7: Determine all the new node voltages from

$$V_i = V_0 - \sum_{j=1}^{b} C_{ij} v_j \text{ , } i = 1, 2, \ldots, n$$

Step 8: Check for convergence based on node voltage differences between consecutive iterations and repeat step 4 to step 7 until the solution converges to a prespecified tolerance of 0.00001 per unit.

6. SOLUTION ALGORITHM

The following steps present the solution algorithm for the optimal placement of sectionalizing switches in radial distribution systems based on the genetic algorithm and reliability cost/worth analysis.

Step 1: Input length of feeder in each section, load level per load point, failure rate, repair time, switch time, replacement time, transfer time, outage cost to customer due to supply outage, switch locations and failure probability of fuses.

Step 2: Input population size and maximum generation.

Step 3: Generate populations 1 and 2 as described in step 1 of Section 2. Each individual in the populations is represented by a string of binary numbers. Binary values of 0 and 1 indicate switch installation and uninstallation, respectively.

Step 4: For each individual, consider a contingency j at load point k (e.g., outage of a line or a transformer) in the network for a load step i. Determine all the affected customers (nk) due to the contingency and the interruption duration r_j. The value of r_j is repair time, replacement time or switching time. Repair time and replacement time are used for the customers who are subjected to long interruptions.

Switching time is used for those to whom the service is restored through alternate supply.

Step 5: Calculate the current in each feeder section and the voltage at each load point using the distribution load flow algorithm presented in Section 5, taking into account load transfer if an alternative supply is available.

Step 6: Obtain the load point interruption cost $C_{jk}(r_j)$ with the customer damage function shown in Figure 1.

Step 7: Calculate the contribution of the contingency to system ECOST using $\sum_{k=1}^{nk} L_{ik} C_{jk}(r_j)\lambda_j$.

Step 8: If $k = nk$, go to step 9. Otherwise, repeat step 5 to step 7 for a next load step.

Step 9: If $j = nj$ (all the contingencies on the primary and the lateral sections at all loads have been considered), go to step 10. Otherwise, repeat step 5 for next contingency.

Step 10: If $i = ni$, go to step 11. Otherwise, repeat step 5 for next load level.

Step 11: Calculate the objective function from the summation of the investment cost, maintenance cost, ECOST and a penalty term. The penalty term is used if the population being considered violates the constraints of line current and bus voltage limits.

Step 12: Do step 4 to step 11 until every individual in populations 1 and 2 are considered.

Step 13: Perform step 3 to step 10 in Section 2.

7. CASE STUDY

The test system in this case study consists of two feeders of PEA designated as KWA01 (stand for Klongkwang01) and KWA06 (stand for Klongkwang06) [8]. These two feeders have 2 feeders and 26 load points shown in Figure 2 and connected with residential customers, small users, medium users, large users, special users and government. Fuses are installed at the tee-point in each lateral. The network data is provided in appendix. Three phase pad mounted sectionalizing switches are considered for the test system. The investment cost of a pad mounted sectionalizing switch is taken as 200,000 Baht. The annual maintenance cost is 2% of the annual investment cost. The life period of the switch is considered to be 20 years and the interest rate as 8%.

Five cases are investigated.

Case 1: Sectionalizing switches are installed along the main feeders at the positions numbered in Figure 2. The fuses at the lateral distributors are assumed to be 100% reliable.

Case 2: This is the same as case 1 except that no sectionalizing switches are installed at the locations numbered in Figure 2.

Case 3: This is the same as case 1 except that the number and locations of sectionalizing switches are determined by the genetic algorithm with 100 generations and 70 populations.

Case 4: The same as case 3 except that the fuses are 90% reliable.

Case 5: This is the same as case 3 except that a seven step load duration curve shown in Figure 3 instead of the average load is applied to each load point with a load increment of 10%. The corresponding step probabilities are 0.0132, 0.1114, 0.1651, 0.2328, 0.2147, 0.2263, 0.0365 [5].

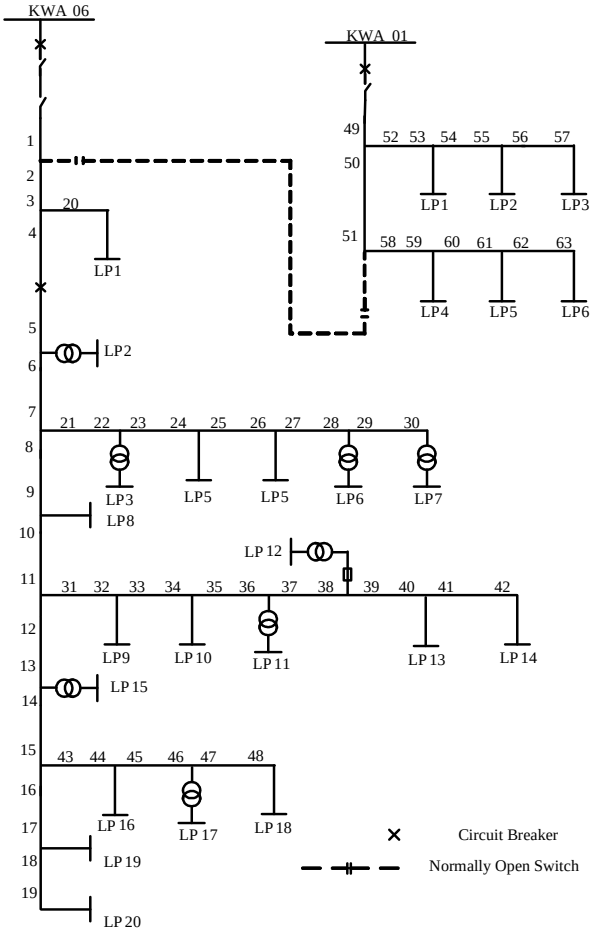

Fig. 2. Feeder KWA01 and KWA06.

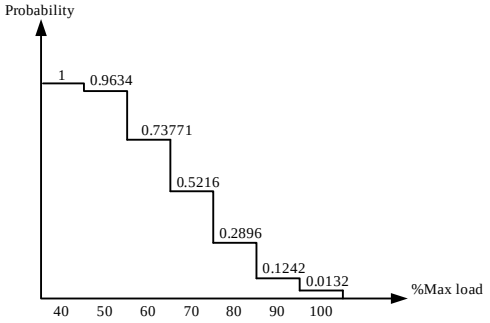

Fig. 3. Seven Step Load Duration Curve.

Table 1. Results of Five Cases

Case	SAIFI	SAIDI	ENS	ECOST	Total Cost	No. of Switches	Locations
1	7.506	17.416	35,554.40	1,696,498	3,005,474	63	1-63
2	7.506	26.651	72,295.92	2,940,815	2,940,815	0	-
3	7.506	19.421	37,526.77	1,759,361	1,925,580	8	1,4,12,16,21,49,50,51
4	7.531	19.446	37,632.06	1,764,575	1,930,794	8	1,4,12,16,21,49,50,51
5	7.506	19.284	48,050.84	2,303,629	2,469,848	9	1,4,12,16,21,31,49,50,51
6	7.506	15.990	27,543.02	1,625,078	1,791,297	8	1,4,12,15,21,49,50,51
7	7.506	18.936	41,185.17	2,160,063	2,472,774	8	1,4 (automated),12,16,21,49,50,51

Units: SAIFI – interruptions/customer.year SAIDI – hour/customer.year Total Cost – Baht/year

ENS – kWh/year Expected Outage Cost – Baht/year

The simulation results for the five cases are shown in Table 1. In case 1, the system requires 63 sectionalizing (63 positions) with a total cost of 3,005,474 Baht. Without any sectionalizing switches in case 2, the total cost is 2,940, 815 Baht. We can see that the total costs of the two cases are not much different. The investment cost is higher in case 1 but lower in case 2. The expected outage cost is lower in case 1 but higher in case 2. These two cases represent two extremes from the utility's and customers' point of view; to be precise, the customers are served with a very good electric supply in case 1 whereas case 2 would be favored by the utility. Nevertheless, there exists the optimum balance between the two cases. Such a balance can be found in case 3, where 8 sectionalizing switches at locations 1, 4, 12, 16, 21, 49, 50, 51 (see Fig. 4.) are required with a total cost of 1,925,580 Baht. Note that the first three cases have the same SAIFI because sectionalizing switches have nothing to do with system failure frequency but they do affect SAIDI and ENS.

If the fuses in the lateral are considered 90 % reliable as in case 4, its SAIFI, SAIDI, ENS, ECOST and total cost are increased, compared with those of case 3. The number and locations of sectionalizing switches remain, however, unchanged. If the seven step load model are applied to each load point for case 5, 9 sectionalizing switches in total should be installed, namely one additional switch is needed at location 31.

8. IMPACT OF AUTOMATED DEVICES

It is seen from the case study that supply restoration becomes crucial for reliability improvement. In the other words, the sooner the restoration time, the better the system reliability. Fast restoration can be achieved by automated devices, which can be remotely activated (minute or less) after a fault has occurred. The impact of automated devices will be demonstrated by two more cases, case 6 and case 7, that are an extension from case 3 of the case study in section 7.

Case 6 is the same as case 3 except that the normally open switch, by which the load can be transferred from KWA01 to KWA06 and vice versa, has a switching time of 1 minute (0.0167 hour). The simulation result is shown in Table 1. The difference between the results of the two cases is that the switch at location 16 in case 3 is moved to location 15 in case 6. Although the optimal patterns of sectionalizing switches for both cases are similar, the total cost of case 6 is significantly reduced, mainly because of a decrease in the ECOST.

In the case study, sectionalizing switches considered so far are manually operated. In fact, system reliability can be further improved by automated sectionalizing switches. Most distribution systems either have only manually operated devices (no automated devices) or are partially automated with a combination of manual and automated devices. A system with partial automation can be two-stage upstream and downstream restorations as shown in Figs. 4 and 5, respectively [9].

In Fig. 4, the breaker will clear the fault. The automated switch is opened allowing section A to be quickly restored and the manual sectionalizing switch will later be opened to restore the customers on section B. In case of downstream restoration in Fig. 5, after the fault is cleared, the automated switch in the downstream path immediately prior to section A will be opened, allowing section A to be supplied from a normally open point (n.o.1). Section B remains without power until the first manual sectionalizing switch is opened and the normally open point in the downstream path (n.o.2) is closed.

If automated sectionalizing switches become a candidate in case 3 of the case study with a switching time of 1 minute and an investment cost of 400,000 Baht (i.e., twice the cost of the manually operated switch), no sectionalizing switch is required. However, if we suppose that the load at LP1 were increased from 3.13075 MW to 4 MW, 8 sectionalizing switches would be required as indicated in case 7 of Table 1. It can be observed from the results that the system should replace the switch of manual type in case 3 at location 4 with that of automation type in case 7. This replacement is reasonable because the load at LP1 is so high enough that fast service restoration can help it reduce the customer interruption cost. Therefore, it is worth investing the automated sectionalizing switch.

Note from the results of cases 3 to 7 that many of the switches are installed at common locations. To be

precise, a sectionalizing switch is installed at or near a main feeder. This is logical because the switch can cover several sections of the feeder and laterals downstream to the switch, and therefore it can isolate any faults that may occur on those sections.

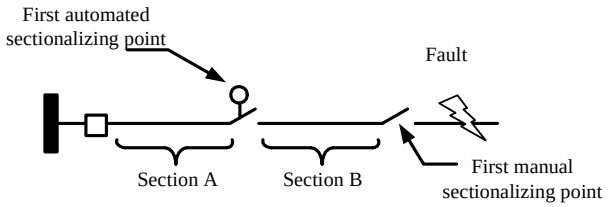

Fig. 4. Two-Stage Upstream Restoration.

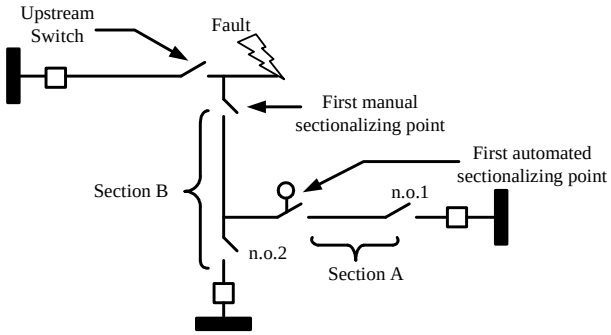

Fig. 5. Two-Stage Downstream Restoration.

9. CONCLUSION

The optimal placement of sectionalizing switches in a radial distribution system has been presented. The objective function is to minimize the sum of investment cost, maintenance cost and customer outage cost, subject to line current and bus voltage limits. The first two costs depend directly upon the number of installed sectionalizing switches that are determined from algorithm. The last cost is obtained from reliability cost and worth analysis. A distribution load flow algorithm is developed based on a constant sparse upper triangle matrix to calculate line current and load-point voltages used to penalize populations that violate the constraints of line current and bus voltage limits in the optimization problem. A case study on a distribution network of the PEA system reveals that methodology provides an optimum decision between economic and reliability consideration. The impact of fast service restoration from the automated normally open switch and the automated sectionalizing switch is also investigated.

REFERENCES

[1] Billinton, R. and Jonnavithula, S. 1996. Optimal Switching Device Placement in Radial Distribution Systems. *IEEE Trans. Power Systems*, 11(3): 1646-1651.

[2] Winston, W. and Venkataramanan, M.A. 2003. *Introduction to Mathematical Programming*. California: Thomson.

[3] Zbigniew, M. 1996. *Genetic Algorithm + Data Structhms = Evolution Programs*. New York: Springer.

[4] Billinton, R. 1984. *Reliability Evaluation of Power Systems*. London England: Pitman.

[5] Energy Policy and Planning Office, Ministry of Energy, 2001. Thailand.

[6] Aravindhababu, P., Ganapathy, S. and Nayar, K.R. 2001. A Novel Technique for the Analysis of Radial Distribution Systems. *Electrical Power & Energy System*, 23: 167-171.

[7] Provincial Electricity Authority Thailand.

[8] Goel, L. and Billinton, R. 1991. Procedure for Evaluating Interrupted Energy Assessment Rates in an Overall Electric Power System. *IEEE Trans. Power Systems*, 6(4): 1398-1403.

[9] Brown, R.E. and Hanson, A.P. 2001. Impact of Two-Stage Service Restoration on Distribution Reliability, *IEEE Trans. Power Systems*, 16(4): 624-629.

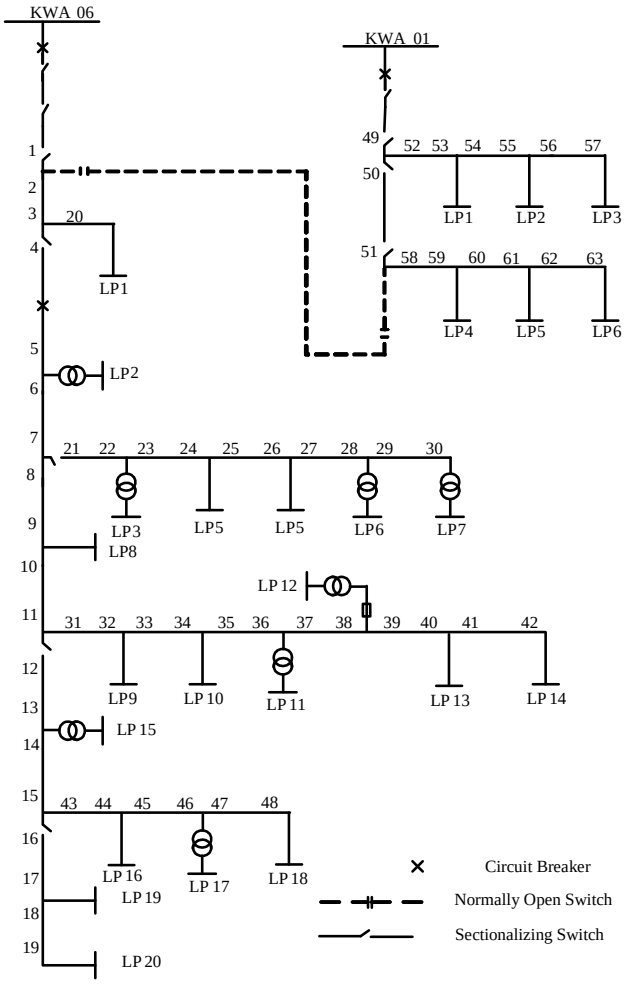

Fig. 6. Optimal Placement of Sectionalizing Switches in Test System.

APPENDIX

Table A1. Customer Data of Feeder KWA01

Load Point	Number of Customer	Type	Demand (MW)	
			Average	
LP1	1	Large Business	0.7000	LP1
LP2	1	Large Business	0.7000	LP2
LP3	1	Medium Business	0.2205	LP3
LP4	1	Medium Business	0.0350	LP4
LP5	1	Medium Business	0.1050	LP5
LP6	1	Medium Business	0.1050	LP6

Table A2. Customer Data of Feeder KWA01

Load Point	Number of Customer	Type	Demand (MW)	
			Average	Maximum
LP1	1	Large Business	3.13075	LP1
LP2	105	Residence	0.0325	LP2
LP3	31	Residence	0.00975	LP3
LP4	1	Medium Business	0.11025	LP4
LP5	31	Residence	0.00975	LP5
LP6	31	Residence	0.00975	LP6
LP7	21	Residence	0.00650	LP7
LP8	1	Government	0.04550	LP8
LP9	21	Residence	0.00650	LP9
LP10	1	Small Business	0.01050	LP10
LP11	1	Medium Business	0.17500	LP11
LP12	31	Residence	0.00975	LP12
LP13	84	Residence	0.02600	LP13
LP14	1	Medium Business	0.05600	LP14
LP15	1	Medium Business	0.17500	LP15
LP16	1	Government	0.02275	LP16
LP17	1	Government	0.01750	LP17
LP18	1	Government	0.03500	LP18
LP19	21	Residence	0.00650	LP19
LP20	1	Government	0.00975	LP20

Table A3. Reliability Data of Feeder KWA01 and KWA06

Component	*l*	*r*	*s*
Transformers	0.0150	200	-
Lines	0.37	5	1.06

where *l* = failure rate

r = repair time (hour)

s = switching time (hour)

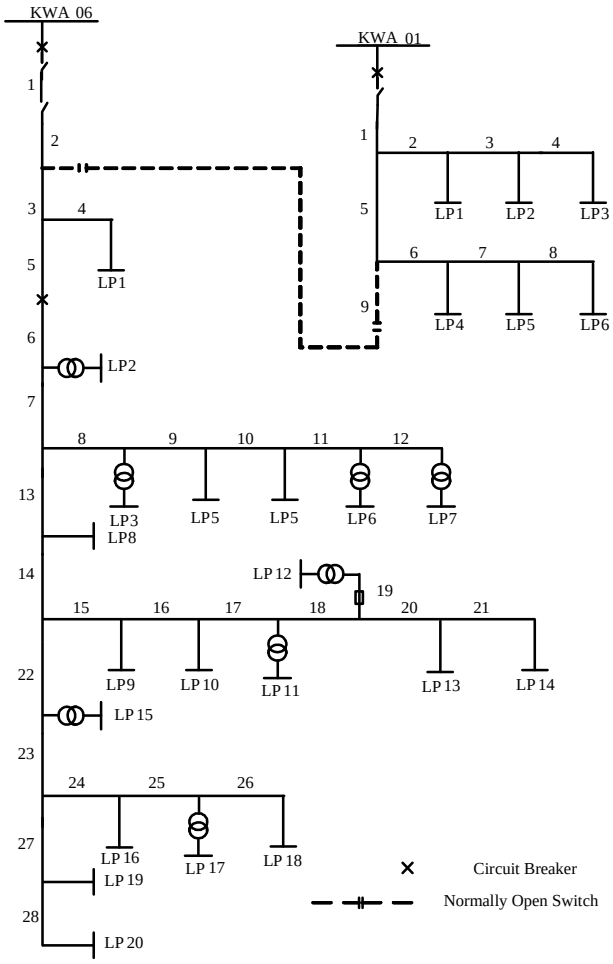

Fig. A1. Feeder KWA01 and KWA06.

Table A4. Type and Length of Feeder KWA01

Section	Length (km)	Type
1	1.0760	SAC 185
2	0.9740	SAC 185
3	0.0066	SAC 185
4	0.1960	SAC 185
5	2.1750	SAC 185
6	0.4150	SAC 185
7	0.0610	SAC 185
8	0.0130	SAC 185
9	0.9800	SAC 185

Table A5. Type and Length of Feeder KWA06

Section	Length (km)	Type
1	8.7400	SAC 185
2	0.3830	SAC 185
3	0.4290	SAC 185
4	0.2890	SAC 185
5	3.0060	SAC 185
6	0.1900	ACSR 50
7	1.0690	ACSR 50
8	0.8540	ACSR 50
9	0.0170	ACSR 50
10	0.2220	ACSR 50
11	0.5180	ACSR 50
12	0.0810	ACSR 50
13	0.5080	ACSR 50
14	0.0640	ACSR 50
15	0.3120	ACSR 50
16	0.0510	ACSR 50
17	0.4660	ACSR 50
18	0.0910	ACSR 50
19	0.4100	ACSR 50
20	0.1660	ACSR 50
21	0.3190	ACSR 50
22	0.5050	ACSR 50
23	0.1300	ACSR 50
24	0.3940	ACSR 50
25	0.6930	ACSR 50
26	0.4300	ACSR 50
27	0.2910	ACSR 50
28	0.0910	ACSR 50

Pure Butane as Refrigerant in Domestic Refrigerator Freezer

M.A. Sattar, R. Saidur and H.H. Masjuki

Abstract— *This paper presents an experimental investigation on the performance of a domestic refrigerator using pure butane as a refrigerant. A domestic refrigerator designed to work with R-134a as refrigerant was used as test unit to assess the possibility of pure butane as refrigerant. The experiments are conducted with the refrigerants under the same no load condition at a surrounding temperature of 25°C and 28°C. The refrigeration capacity, the compressor power, the coefficient of performance (COP), condenser duty and heat rejection ratio were investigated. The performance parameter and power consumption of the refrigerator when R-134a was used as refrigerant is considered as baseline. The performance of pure butane is compared with the performance of R-134a. The compressor consumes 2.08kWh/day and 2.25kWh/day when R-134a is used refrigerant but when butane is used it consumes 2.197kWh/day and 2.199kWh/day at 25°C and 28°C ambient temperature respectively. The result shows a better performance of butane than R-134a. The results support the possibility of using butane as an alternative to R-134a in domestic refrigerators, without any modification of the domestic refrigerator.*

Keywords— **Butane, Refrigeration capacity, COP, Condenser duty.**

1. INTRODUCTION

Natural ice was harvested, distributed and used in both commercial and home applications in the mid-1800s to refrigerate food. The idea that cold could be produced by the forced evaporation of a volatile liquid under reduced pressure had been previously pursued by William Cullen in the eighteenth century. These same volatile liquids could be condensed from a vapor state by application of cooling and compression was also known by the 1800s. Combining these two ideas led to the development of what would ultimately become the dominant means of cooling –the vapor compression refrigerating system. Since the invention of the vapor compression refrigeration system in the middle of the 18th century and its commercial application at the end the 18th century, the application of refrigeration has entered many fields. The application includes the preservation of food and medicine, air-conditioning for comfort and industrial processing. Stratospheric ozone absorbs the sun's high-energy ultraviolet rays and protects both humans and other living things from exposure to ultraviolet radiation. Results from many researches show that this ozone layer is being depleted. The general consensus for the cause of this event is that free chlorine radicals remove ozone from the atmosphere, and later, chlorine atoms continue to convert more ozone to oxygen. The presence of chlorine in the stratosphere is the result of the migration of chlorine containing chemicals. The chlorofluorocarbons (CFCs) and hydrochloro-fluorocarbons (HCFCs) are a large class of chemicals that behave in this manner. These chemicals have many suitable properties, for example, non-flammability, low toxicity and material compatibility that have led to their common widespread use by both consumers and industries around the world, especially as refrigerants in air conditioning and refrigerating systems [1,4]. Scientist and researcher are searching the environment benign refrigerant for the domestic refrigerator and freezer. Hydrocarbon especially propane, butane and isobutene are proposed as an environment benign refrigerant. Hydrocarbons are free from ozone depletion potential and have negligible global warming potential. Lee and Su (2002) conducted an experimental study on the use of isobutene as refrigerant in domestic refrigerator. The performance was comparable with those of CFC-12 and HCFC-22 was used as refrigerant. Akash and Said (2003) studied the performance of LPG from local market (30%propane, 55% n-butane and 15% isobutene by mass) as an alternative refrigerant for CFC-12 in domestic refrigerator with masses of 50g, 80g and 100g. The result showed that a mass charge of 80g gave the best performance. S. Devotta *et al* (2001) selected HFC-134a, HC-290, R-407C, R-410A, and three blends of HFC-32, HFC-134a and HFC-125 and found that HFC-134a offers the highest COP, but its capacity is the lowest and requires much larger compressors. The characteristics of HC-290 are very close to those of HCFC-22, and compressors require very little modification. Therefore, HC-290 is a potential candidate provided the risk concerns are mitigated as had been accomplished for refrigerators. S. J. Sekhar *et al* (2004) investigated an experiment to retrofit a CFC12 system to eco-friendly system using of HCFC134a/HC290/HC600a without changing the mineral oil and found that the new mixture could reduce the energy consumption by 4 to 11% and improve the actual COP by 3 to 8% from that

M.A. Sattar (corresponding author) is with the University of Malaya, 50603 Kuala Lumpur, Malaysia. Tel: +60-162482734; Fax: +60-379675317; E-mail: sattar106@yahoo.com.

R. Saidur is with the University of Malaya, 50603 Kuala Lumpur, Malaysia. E-mail: saidur@um.edu.my.

H.H. Masjuki is with the University of Malaya, 50603 Kuala Lumpur, Malaysia. E-mail: masjuki@um.edu.my.

of CFC12. S. J. Sekhar *et al* (2005) investigated refrigerant mixture of HCFC134a/HC in two low temperature system (domestic refrigerator and deep freezer) and two medium temperature system (vending machine and walk in cooler) and found that the HCFC134a/HC mixture that contains 9% HC blend (by weight) has better performance resulting in 10-30% and 5-15% less energy consumption (than CFC) in medium and low temperature system respectively. Hydrocarbons (HCs) are an environmentally sound alternative for CFCs and HFCs. HCs as a refrigerant have been known and used since the beginning of this century. The development of the inert CFCs in the 1930s put the HC technology in the background. CFCs have been applied since then in numerous refrigeration equipments. Eventually the damaging aspects of CFCs became clear and solutions for the problem had to be sought [14]. There is currently little information on the application of Hydrocarbon as refrigerant in the refrigerator with out modification. In this experiment a domestic refrigerator design to work with HFC-134a were investigated without modification. The experiments were conducted with R-134a and pure butane. According to the ISO standard, the test period shall be at least 24 h long with no door openings. Relative humidity should be kept within 45%–75% inside the chamber. Environment temperature should be kept within 25±0.5°C to 32±0.5°C [15]. So in this experiment the environment temperature was considered at 25°C and 28°C and relative humidity was maintained at 60%.

2. EXPERIMENTAL SETUP AND TEST PROCEDURE

2.1 Experimental methodology and apparatus

The schematic diagram of the test unit and apparatus is shown in Figure 1. The thermocouple sensors (T-type) and pressure sensors were fitted at inlet and outlet of the compressor, condenser, and evaporator as shown in Figure 1. Thermocouples and pressure sensors were interfaced with a HP data logger via a PC through the GPIB cable for data storage and analysis.

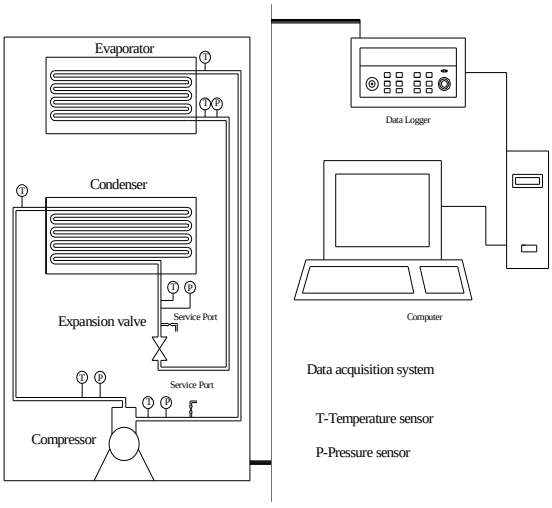

Fig. 1. Schematic diagram of the test unit and apparatus.

Service port is installed at the inlet of expansion valve and compressor for charging and recovering the refrigerant is shown in Figure 1. Yellow jacket 4cfm vacuum pump was used to evacuate the system through this service port. Yellow jacket Digital electronic charging scale has been used to charge the system. A power meter was connected with compressor to measure the power consumption. The specification of the refrigerator is shown in Table 1.

Table 1. Technical specifications of refrigerator freezer test unit

SPECIFICATIONS	
Freezer Capacity (liter)	80
Fresh Food Compartment Capacity (liter)	220
Power Rating (W)	160
Current rating (A)	0.9
Voltage (V)	220
Frequency (Hz)	50
No of door	2
Refrigerant type	134a(CF3CH2F)
Defrost system	Auto Defrost

2.2 Test procedure

The refrigerator has been fitted with the pressure sensors and thermocouples. The system was evacuated with the help of vacuum pump to remove the moisture. The system was charged with the help of digital electronic charging scale after evacuation. The pressure transducer and thermocouple were connected with the data logger. The data logger is interfaced with the computer and software has been installed to operate the data logger from the computer. The data logger was set to scan the data from the temperature sensor and pressure sensor at an interval of 15 minutes within 24 hours. A power meter was connected with the refrigerator and interfaced with the computer. Power meter software was installed in the computer to operate from the computer. The power meter stores the power consumption of the refrigerator at an interval of one minute within 24 hours. The pressure and temperature from the data logger was used to determine the enthalpy of the refrigerant using REFPROP7 software. All equipment and test unit was placed inside the environment control chamber. The temperature and humidity inside the chamber was controlled. The dehumidifier has been used to maintain humidity. The unit can maintain humidity from 60% to 90% with an accuracy of ±5%. The humidity has been maintained at 60% RH for all the experiment. The temperature inside the chamber was maintained at 25°C and 28°C. The experiment has been conducted on the domestic refrigerator with no load and closed door condition.

3. RESULTS AND DISCUSSIONS

3.1 Power consumption by the compressor when different refrigerants were used

The energy consumption by the HFC134a and pure butane are shown in the Table 2.

Table 2. Energy consumption by compressor at 25°C and 28°C

Refrigerant used	Room temperature, 25°C	Room temperature, 28°C
	Energy consumption, kWh/day	Energy consumption, kWh/day
HFC134a	2.077	2.254
Butane	2.197	2.199

3.2 Effect of evaporator and condenser temperature on co-efficient of performance

The COP against inlet refrigerant temperature of the evaporator is plotted at 25°C and 28°C ambient temperatures and shown in Figures 2 and 3. The Figures 4 and 5 show a progressive increase in COP as the evaporating temperature increases. The COP of the domestic refrigerator is plotted against condenser temperature of the refrigerator and shown in Figures 6 and 7. The Figures 4 and 5 show that COP increases as the temperature of the condenser decrease.

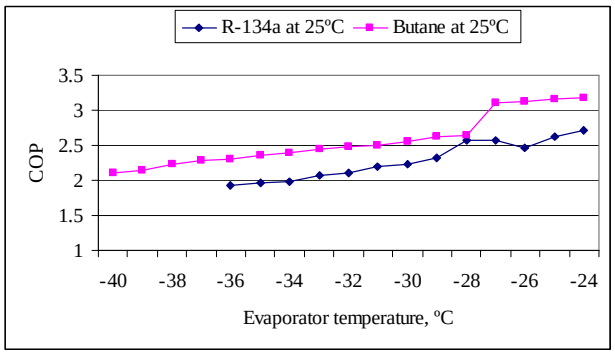

Fig. 2. Effect of evaporator temperature on co-efficient of performance.

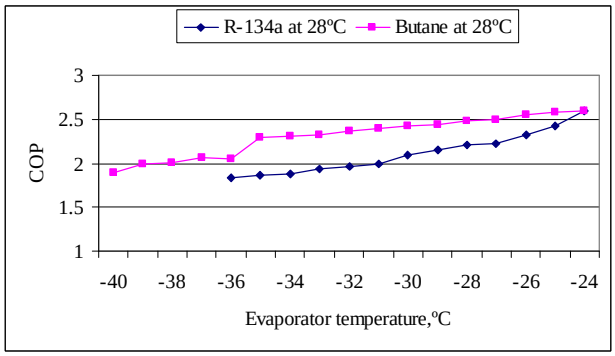

Fig. 3. Effect of evaporator temperature on co-efficient of performance.

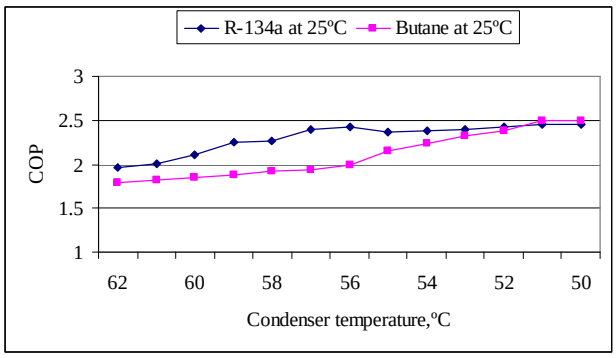

Fig. 4. Effect of condenser temperature on co-efficient of performance.

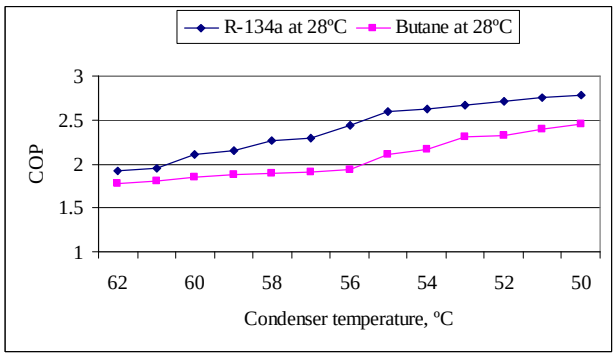

Fig. 5. Effect of condenser temperature on co-efficient of performance.

3.3 Effect of evaporator temperature on refrigerating effect and compressor work.

The refrigerating effect and inlet refrigerant temperature is shown in Figures 6 and 7.The refrigerating effect increases as the temperature of the evaporator increases as shown in Figures 6 and 7. The refrigerant effect when pure butane is used is higher than R-134a because the value of enthalpy of the pure butane is higher than that of HFC134a.

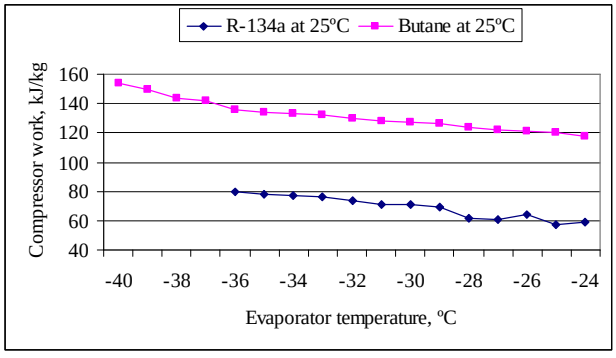

Fig. 8. Effect of evaporator temperature on work of compression.

The work of compression and inlet refrigerant temperature is shown in Figures 8 and 9. The work of compression increases as the temperature of the evaporator decreases. This is due to the fact that when

the temperature of the evaporator decreases the suction temperature also decreases. At low suction temperature, the vaporizing pressure is low and therefore the density of suction vapor entering the compressor is low. Hence the mass of refrigerant circulated through the compressor per unit time decreases with the decreases in suction temperature for a given piston displacement. The decreases in the mass of refrigerant circulated increases in work of compression.

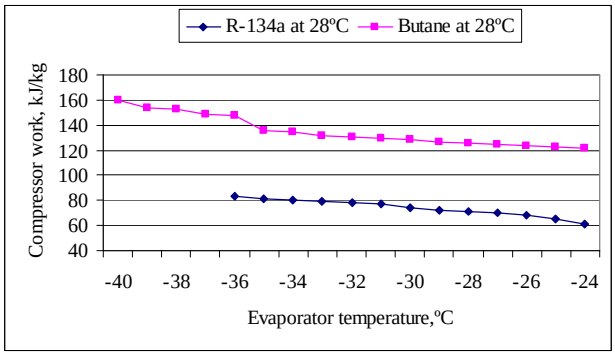

Figure 9 effect of evaporator temperature on work of compression.

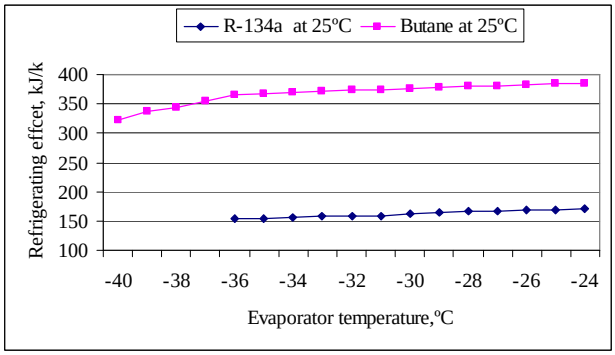

Fig. 6. Effect of evaporator temperature on refrigerating effect.

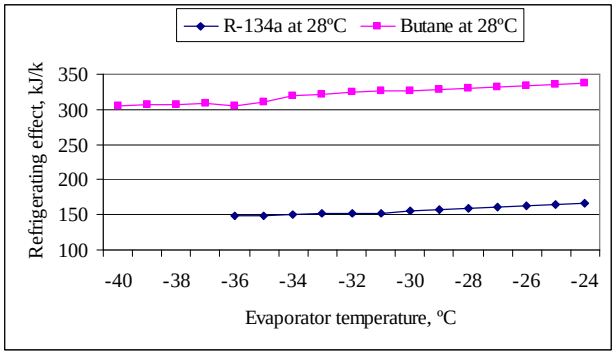

Fig. 7. Effect of evaporator temperature on refrigerating effect.

3.4 Effect of evaporator temperature on condenser duty for different refrigerants

The function of the condenser is to remove heat of the hot vapor refrigerant discharged from the compressor. The heat from the hot refrigerant is removed by transferring heat to the wall of the condenser tubes and then from the tubes to the condensing medium. The condenser duty and evaporator temperature is shown in Figures 10 and 11. The figures show that the condenser duty increases as the temperature of the evaporator decreases.

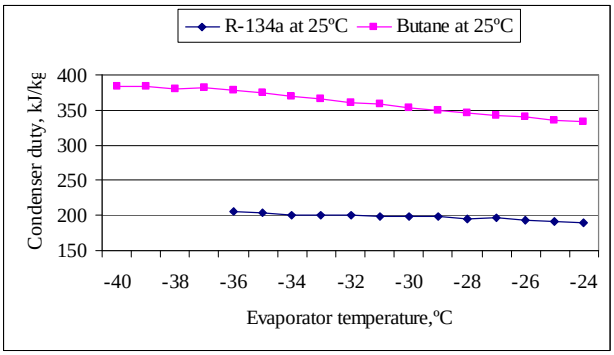

Fig. 10. Effect of evaporator temperature on condenser duty.

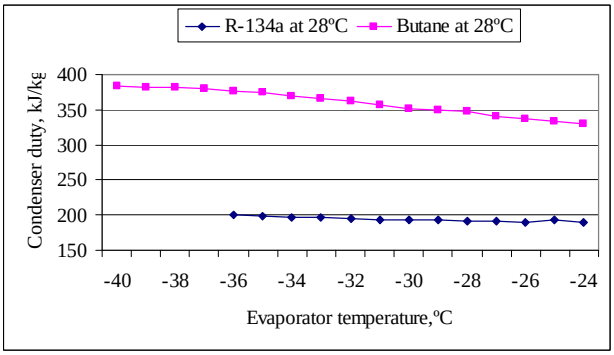

Fig. 11. Effect of evaporator temperature on condenser duty for iso-butane.

3.5 Heat rejection ratio for different refrigerant

The required rate of heat transfer in the condenser is predominantly a function of the refrigerating capacity and the temperatures of evaporation and condensation. A term often used to relate the rate of heat flow at the condenser to that of the evaporator is the heat-rejection ratio. Heat rejection ratio at the condenser temperature is shown in Figures 12 and 13.

4. CONCLUSIONS

This project invested an ozone friendly, energy efficient, user friendly, safe and cost-effective alternative refrigerant for HFC134a in domestic refrigeration systems. The following conclusion can be drawn based on the result obtained after the successful investigation.

- The co-efficient of performance of pure butane is comparable with the co-efficient of performance of HFC134a.
- The energy consumption of the pure butane is about similar to the energy consumption of

refrigerator when HFC134a is used as refrigerant.

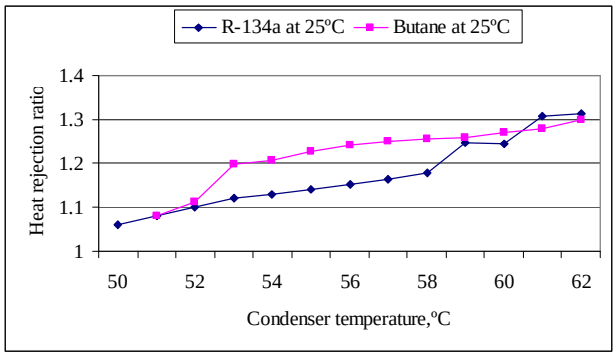

Fig. 12. Effect of condenser temperature on heat rejection ratio

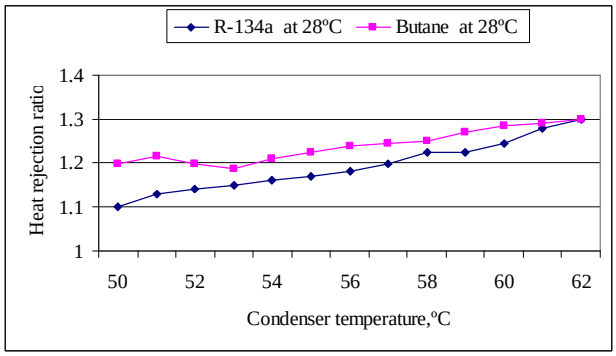

Fig. 13. Effect of condenser temperature on heat rejection ratio.

- Pure butane offers lowest inlet refrigerant temperature of evaporator. So for the low temperature application pure butane is better than HFC134a.
- The amount of charge of pure butane is less than the manufacturer recommended charge of HFC134a in the present test unit. The domestic refrigerator was charged with 140gm of HFC134a and 70gms of butane. This is an indication of better performance of the HC as refrigerant.
- The experiment was performed on the domestic refrigerator purchased from the market, the components of the refrigerator was not changed or modified. This indicates the possibility of using butane in the existing refrigerator system without modification of the components.
- Chemical and thermodynamics properties of Hydrocarbon meet the requirement of a good refrigerant. Hydrocarbons are environmentally friendly. Hydrocarbon is cheaper than the R-134a and easily available. Some standards allow the use HC as refrigerant if small amount of refrigerant is used.

ACKNOWLEDGEMENTS

The authors gratefully acknowledge the financial support by the Ministry of Science Technology and Innovation (MOSTI), Malaysia to carry out this research project. The project was funded under the project IRPA No: 03-02-03-1011.

REFERENCE

[1] Radermacher, R., Kim, K. 1996. Domestic refrigerator: recent development. *International journal of refrigeration*, 19: 61-69.

[2] Lee, Y.S. Su, C.C. 2002. Experimental studies of isobutene (R600a) as refrigerant in domestic refrigeration system. *Applied Thermal Engineering*, 22: 507-519.

[3] Maclaine-cross, I.L. 2004. Usage and risk of hydrocarbon refrigerants in motor cars for Australia and the United States. *International Journal of Refrigeration*, 27(4): 339-345.

[4] Bilal A. Akash, Salem A. Said, 2003. Assessment of LPG as a possible alternative to R-12 in domestic refrigerators. *Energy conversion and Management*, 44: 381-388.

[5] Alsaad, M.A., Hammad, M.A. 1998. The application of propane/butane mixture for domestic refrigerators. *Applied Thermal Engineering*, 18: 911-918.

[6] Somchai Wongwises and Nares Chimres, 2005. Experimental study of hydrocarbon mixtures to replace HFC-134a in a domestic refrigerator. *Energy conversion and management*, 46: 85-100.

[7] Tashtoush, B., Tahat, M., Shudeifat, M.A. 2002. Experiment study of new refrigerant mixtures to replace R12 in domestic refrigerator. *Applied Thermal Engineering*, 22: 495-506.

[8] Devotta, S., Wagmare, A.V. Sawant, N.N. Domkundwar, B.M. 2001. Alternatives to HFC-22 for air conditioners. *Applied Thermal Engineering*, 21: 703-715.

[9] Joseph Sekhar S., Mohan Lal D., Renganarayanan, S. 2004. Improved energy efficiency for CFC domestic refrigerators with ozone-friendly HFC134a/HC refrigerant mixture. *International Journal of thermal Science*, 43:307-314.

[10] Sekhar, S.J., Lal, D.M. 2005. HFC134a/HC600a/ HC290 mixture a retrofit for CFC12 system. *International journal of refrigeration*, 28: 735-743.

[11] Granryd, E. 2001. Hydrocarbons as refrigerants - an overview. *International Journal of Refrigeration*, 24: 15-24.

[12] Palandre, L., Zoughaib, A., Clodic, D. and Kuijpers, L. 2003. Estimation of the world-wide fleets of refrigerating and air-conditioning equipment in order to determine forecasts of refrigerant emissions – *The Earth Technology Forum*, Washington.

[13] Devotta, S., Kulkarni, M.M., Sawant, N.N., Patil, P.A., and Sane, N.K. 1998. Compressor life tests with HC refrigerants. *Proc. IIF/IIR Gustav Lorentzen Conf.*, Oslo, Norway, 668-75.

[14] Study on the Potential for Hydrocarbon Replacements in Existing Domestic and Small

Commercial Refrigeration Appliances. United Nations Publication ISBN 92-807-1765-0.

[15] Masjuki, H.H., Saidur, R., Choudhury, I.A., Mahlia, T.M.I., Ghani, A.K and Maleque, M.A. 2001. The applicability of ISO household refrigerator–freezer energy test specifications in Malaysia. *Energy*, 26: 723–737.

Sliding Mode Control for Wind Turbine with Doubly Fed Induction Generators

Watthana Seubkinorn and Bunlung Neammanee

Abstract*— *The main objective of a wind energy conversion system is to converse energy from the wind into electrical energy as much as possible. The power coefficient characteristic of a wind turbine has a single maximum at a specific value of the tip speed ratio. The wind turbine should, therefore, operate at the maximum power coefficient. Another important objective for wind turbine operation is to limit the output at the rated value. The paper presents a wind turbine control technique based on a sliding mode control (SMC) for the two control objectives. The simulation result from a case study shows that the SMC has good tracking performance and it can efficiently regulate the maximum peak power.

***Keywords*— Sliding mode control, wind turbine, doubly fed induction generator.**

1. INTRODUCTION

Wind turbines are generally composed of a rotating rotor with three blades. This rotor is the aerodynamic component of the wind turbine. It captures the energy available in the wind, and transfers it to a rotating shaft, located inside the wind turbine nacelle. The shaft is mechanically connected to the electromechanical converter unit. The main objective of a wind energy conversion system is to converse energy from wind into electrical energy with maximum efficiency. The power coefficient characteristic of a wind turbine has a single maximum at a specific value of the tip speed ratio. The wind turbine should, therefore, operate at the optimum power coefficient.

In this paper, the electromechanical converter unit is a gearbox with a doubly fed induction generator (DFIG) shown in Figure 1. The stator winding of the DFIG is directly connected to the grid and its wound rotor is connected with a static Kramer drive. The static Kramer drive topologies have a three phase diode bridge rectifier located in machine side, and a three phase line commutate thyristor inverter are located in line side. The rectifier and inverter are coupled together with an inductor. Power flow can be controlled from the rotor circuit by commanding the firing angle of the thyristor unit in a range between 90 and 180 degrees to be operated in inverting mode. The rotational speed of the rotor must be higher than synchronous speed or operates only at supersynchronous speed to generate electrical power from both the stator and the rotor circuits.

Operating regions is generally classified into four regions as shown in Figure 2, which represents a typical power versus wind speed curve of a wind turbine. The figure indicates three wind velocities on which the four regions are separated based. In the figure, the cut-in velocity is defined as the wind speed at which the turbine starts to generate the power. Below this wind speed, it is not efficient to turn on the turbine. The rated velocity (v_{rated}) is the wind speed at which the turbine reaches its rated turbine power. The cut-out velocity ($v_{cut-out}$) is the maximum wind speed at which the wind turbine can still operate. Beyond this wind speed, the rotor has to be shut down to keep the blades, the electrical generator and other components from reaching damaging level [3-4].

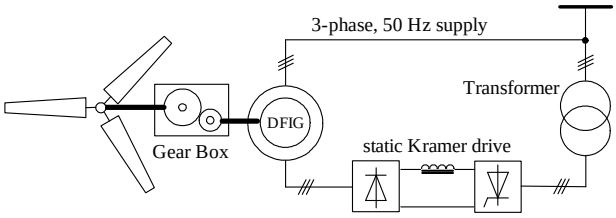

Fig. 1. Schematic diagram of WECS by DFIG with static Kramer drive system.

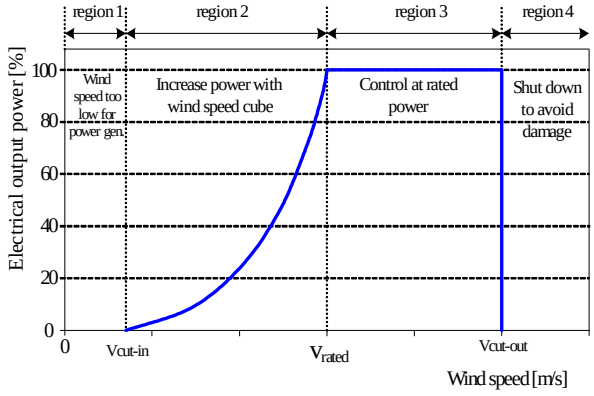

Fig. 2. Operation area of wind turbine.

The operation regions of interest in this paper are regions 2 and 3. Region 2 covers a wind speed range between v_{cut-in} and v_{rated} and is referred as the below rated power region. Because the power generated from a

The authors are with Department of Electrical Engineering, King Mongkut's University of Technology North Bangkok 1518 Bangsue, Bangkok 10800, Thailand. Phone: (+66)2913-2500-24 Ext: 8420; Fax: (+66)2585-7350; E-mail: bln@kmutnb.ac.th, wsk@sau.ac.th.

wind speed in this region is a function of the cube of that wind speed, the main task of a controller is to capture the maximum power output for that wind speed. Region 3 covers a wind speed range between v_{rated} and $v_{cut-out}$ and is referred as the above rated power region. As the mechanical power generated by the rotor is limited, the main task of a controller in this region is to keep output at its rated power [4].

This paper presents a sliding mode control (SMC) developed with a designed control law to force the generator torque to be a linear function of the generator speed around the operating point of maximum power transfer in the below rated wind speed region. In addition, the power is limited by stall regulation in the above rated wind speed region.

2. MATHAMATICAL MODEL OF SYSTEM

The mathematical model of wind turbine is described in section 2.1. The mathematical model of the static Kramer drive and the DFIG are described in section 2.2. Section 2.3 presents the overall system that combines sections 2.1 and 2.2.

2.1. Mathematical Model of Wind Turbine

The power generated from the wind can be expressed by (1). According to Betz's law, an ideal wind turbine would, in theory, extract the 16/27 of this power. However, in practice, due to non-laminar air flow and friction between blade surfaces, the energy capture of the wind turbine is reduced by a factor known as the power coefficient, c_P, given in (2). Another two important characteristics of the wind turbine are the torque coefficient and aerodynamic torque defined in (5).

$$P_w = \frac{1}{2}\rho A v^3 \tag{1}$$

$$c_P(\lambda) = \frac{P_{\text{rotor}}}{P_{\text{wind}}} = \frac{P_{\text{rotor}}}{1/2\rho A v^3} \tag{2}$$

where

$$P_{rotor} = \frac{1}{2}\rho A v^3 c_P(\lambda) \tag{3}$$

$$\lambda = \frac{R\Omega}{v} \tag{4}$$

$$T_a = \frac{1}{2}\rho\pi R^3 v^2 c_T(\lambda) \tag{5}$$

where

$$c_T = \frac{c_P}{\lambda} \tag{6}$$

The main control objective is to maximize energy capture from the wind. Each wind turbine has its own power and torque characteristics. Figure 3 is an example of wind turbine characteristics. As can be seen, the turbine has a single maximum power coefficient, $c_P^{\max}$, at the tip speed ratio λ_0. When the rotor operates at constant speed, the power coefficient will be at maximum at only one wind speed and therefore to achieve the highest annual energy capture. The value of the power coefficient must be maintained at the maximum level all the time [1, 2].

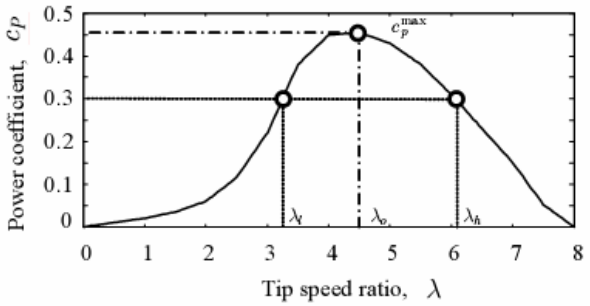

Fig. 3. Power coefficient curve, c_P, versus TSR, λ

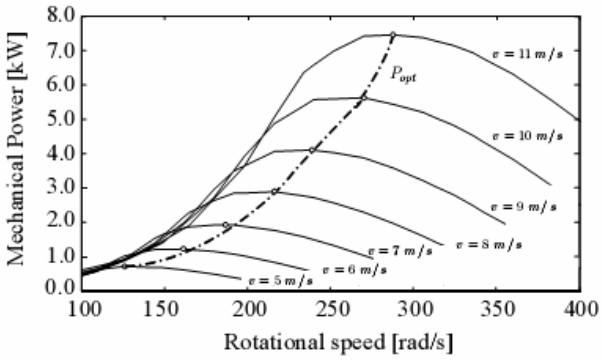

Fig. 4. Aerodynamic power versus rotational speed of generator shaft for various wind velocities.

Figure 4 shows a power-rotational speed curve with seven different wind speeds (5, 6, ..., 11 m/s). Path P_{opt} in the figure indicates the optimum tracking path on which each operating point has $c_P^{\max}$.

2.2. Mathematical Model of DFIG and Static Kramer Drive

Figure 5 shows a per phase equivalent circuit of the DFIG with the static Kramer drive in Figure 1 to analyze electrical power production from mechanical power. The generator torque can be calculated using (7) [2, 6]. The cosine value of firing angle, cos(α), commands the thyristor unit and the rotational speed , Ω, of the DFIG.

$$T_g(\cos\alpha, \Omega) = \frac{3V_s^2 sR_{EQ}(\cos\alpha)\Omega_s^{-1}}{(sR_s + R_{EQ}(\cos\alpha))^2 + (s\omega_s(L_{ds} + L_{dr}))^2} \tag{7}$$

where

$$R_{EQ} = s\frac{sR_B + (\cos\alpha)^2 R_s + \cos\alpha\sqrt{\Gamma}}{s^2 - (\cos\alpha)^2} \tag{8}$$

$$\Gamma = (R_B + sR_s)^2 + (s^2 - \cos^2\alpha)(\omega_s(L_{ds} + L_{dr})) \tag{9}$$

$$R_B = (R_r + 0.55R_f) \tag{10}$$

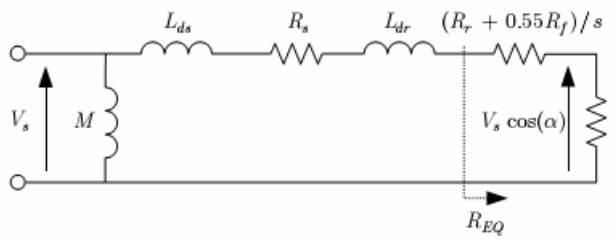

Fig. 5. Equivalent circuit of DFIG with static Kramer drive.

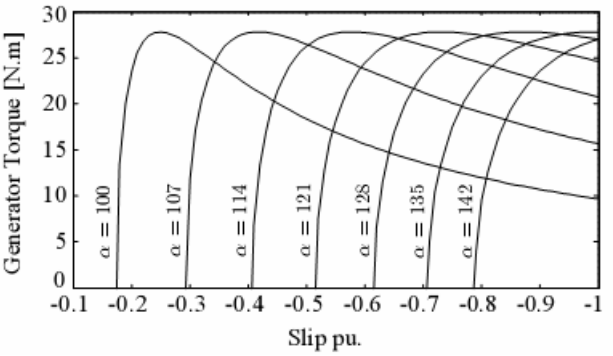

Fig. 6. Torque characteristics versus slip of a DFIG with static Kramer drive for different values of a .

Variable speed operation is achieved by controlling the firing angle of the thyristor, and hence the slip power. Figure 6 shows a plot of generator torque versus slip by varying firing angles from 100 to 142 degrees with an increment of 7 degrees. Note that the range of the firing angle a must be between 90^o and 180^o for inverting mode operation.

Electrical power output, P_E , of the DFIG is affected by its efficiency as given in (11).

$$P_E(\cos\alpha,\Omega) = \eta(\cos\alpha,\Omega)\cdot\Omega\cdot T_G(\cos\alpha,\Omega) \tag{11}$$

where

$$\eta(\cos\alpha,\Omega) = \frac{\Omega_S(1-\cos\alpha)}{\Omega} \tag{12}$$

2.3 Mathematical Model of System

The torque balance of the system is

$$T_a = J\dot{\Omega} + B\Omega + T_g \tag{13}$$

By neglecting the effects of friction and stiffness of the transmission shaft and mechanical losses, the dynamic model can be described by the following equation [10]:

$$\dot{\Omega} = f(\cos\alpha, v, \Omega) = \frac{1}{J}\cdot[T_a(\Omega, v) - T_G(\cos\alpha,\Omega)] \tag{14}$$

Figure 7 shows electrical power from the wind captured by the turbine blades versus rotational speed at 7 different wind velocities. The electrical power is limited by two boundary lines $P_E(\Omega,0)$ and $P_E(-1,\Omega)$. These two lines present the lower and upper limits of the firing angle between 90 and 180 degrees, respectively.

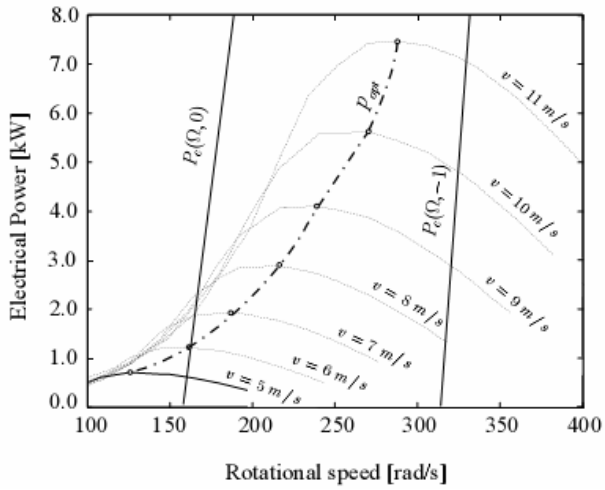

Fig. 7. Aerodynamic and generator power versus rotational speed of generator shaft for various wind velocity.

3. VARIABLE STRUCTURE CONTROL

3.1 Sliding Surface Design

For maximum peak power tracking, the sliding surface can be defined normalized power error in (15). The control objective is to drive the normalized power error to be zero [6].

$$y = h(\cos\alpha,\Omega) = \frac{P_E(\cos\alpha,\Omega)}{P_R} - 1 \tag{15}$$

Let $$u = \cos\alpha \tag{16}$$

Differentiating (15) yields:

$$\dot{y} = \frac{\partial h(u,\Omega)}{\partial u}\cdot\frac{du}{dt} + \frac{\partial h(u,\Omega)}{\partial\Omega}\cdot\frac{d\Omega}{dt} \tag{17}$$

Therefore, the following discontinuous dynamics is imposed.

$$\dot{y} = -W\cdot\mathrm{sign}(y), W > 0 \tag{18}$$

From (17), let

$$L_f h = \frac{\partial h(u,\Omega)}{\partial\Omega}\cdot\frac{d\Omega}{dt} \tag{19}$$

Substituting (19) into (17), $\dot{u}$ is calculated from

$$\dot{u} = -\left(\frac{\partial h(u,\Omega)}{\partial u}\right)^{-1}\cdot[L_f h - \dot{y}] \tag{20}$$

Substituting (18) into (20), $\dot{u}$ is calculated from

$$\dot{u} = -\left(\frac{\partial h(u,\Omega)}{\partial u}\right)^{-1}\cdot[L_f h + W\cdot sign(h(u,\Omega))] \tag{21}$$

Note that from (16) with $90^o < \alpha < 180^o$, then $-1 < u < 0$.

With (14)-(21), we can build a control block diagram of the SMC as shown in Figure 8. The SMC control enclosed by the dash line receives the rotational speed, Ω, and the wind speed, *v*, to generate the control parameter, *u*, to control the plant to achieve the control objective.

3.2 Sliding Mode Control in Stall Region

The output power captured from the wind can be limited by stall regulation. The stall effect is a phenomenon that air flow separates at the wind turbine blade's surface. The separation will limit aerodynamic power and can be controlled by the rotational speed. To stall the turbine, its operating point should be moved to the left of the $c_P^{\max}$ in Figure 3. Since the sliding surface designed by (15) has only one control objective (maximum peak power tracking), (15) is modified by adding normalized speed error to take into account power limit.

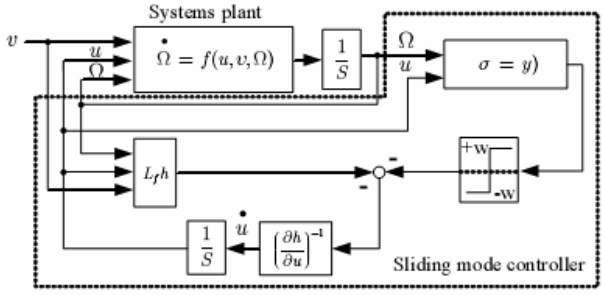

Fig. 8. Block diagram of the dynamic SM controller.

$$\sigma = y - \beta\left(\frac{\Omega}{\Omega_o} - 1\right) \tag{22}$$

$$\dot{\Omega} = \frac{\partial h(u,\Omega)}{\partial u}\cdot\frac{du}{dt} + \left[\frac{\partial h(u,\Omega)}{\partial \Omega} - \frac{\partial \beta\left(\frac{\Omega}{\Omega_o} - 1\right)}{\partial \Omega}\right]\cdot\frac{d\Omega}{dt} \tag{23}$$

Therefore, the following discontinuous dynamics is imposed.

$$\dot{\sigma} = -W \cdot \mathrm{sign}(\sigma), W > 0 \tag{24}$$

From (24), let

$$L_f q = \left[\frac{\partial h(u,\Omega)}{\partial \Omega} - \frac{\beta}{\Omega_o}\right]\cdot\frac{d\Omega}{dt} \tag{25}$$

Substituting (25) into (23), $\dot{u}$ is calculated from

$$\dot{u} = -\left(\frac{\partial h(u,\Omega)}{\partial u}\right)^{-1}\cdot\left[L_f q - \dot{\sigma}\right] \tag{26}$$

Substituting (25) into (23), $\dot{u}$ is calculated from

$$\dot{u} = -\left(\frac{\partial h(u,\Omega)}{\partial u}\right)^{-1}\cdot\left[L_f q + W\cdot sign(\sigma)\right] \tag{27}$$

In order to assure local stability of the closed loop sliding dynamics to any equilibrium point in the stall region, it is sufficient to choose a gain, *b* , satisfying: [6]

$$\beta > \max_{\lambda}(\chi(\lambda)) \tag{28}$$

where

$$\chi(\lambda) = \frac{dC_p(\lambda)}{d\lambda}\cdot\frac{\lambda}{C_p(\lambda)} \tag{29}$$

The coefficient $\chi(\lambda)$ is negative in the normal operating region, positive in the stall region and zero at λ_0.

4. CASE STUDY

4.1 Simulation System

A 7.5 kW wind energy conversion system using a DFIG with a static Kramer drive is considered in simulations (relevant parameters given in appendix). The simulations are based on the control box diagram in Figure 8.

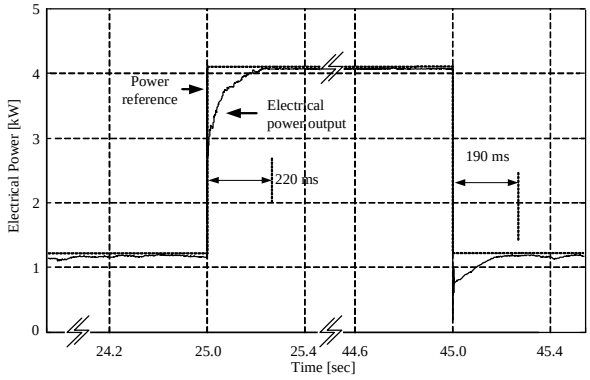

Fig. 9. Dynamic response of maximum peak power tracking to step wind speed.

4.2 Dynamic Response of Maximum Peak Power Tracking

This simulation starts by keeping a wind speed constant at 6 m/s until t = 25 s. The wind speed is then stepped-up to 9 m/s until t = 45 s, and stepped-down to 6 m/s again. The simulation result is shown in Figure 9. We can see that when the wind speed is stepped-up, the SMC uses 220 ms to track the maximum power, and when wind speed is stepped-down, the SMC takes 190 ms to reach the maximum power.

4.3 Maximum Peak Power Tracking without Power Limit

The SM controller uses the sliding surface defined in (15) without power limit. The input wind speed shown in Figure 10 (a) with a power reference from (3). The output power shown in Figure 10 (b), and Figure 10 (c)

is the error between the reference power and output power. Conversely, when the wind speed is greater than 9 m/s, the input power from the wind increases. From Figure 10, if the wind speed is increased at t = 52 s, the output power will be limited owing to $\cos a = 180^{o}$. The corresponding power coefficient and tip speed ratio are shown in Figures 11 (a) and (b), respectively. These figures can confirm that before t = 35 s, c_P is controlled at the maximum value until the wind speed is lower than 5 m/s (35s < t < 52s) During such a period, c_P is not maximum because of the lower limitation of the firing angle (on the left hand side in Figure 7).

4.4 Maximum Peak Power Tracking with Power Limit

This section simulates the sliding surface defined (22). In this mode the wind turbine operates with small values of c_P to limit the input from the wind. Figures 12 (a) and (b) show the input wind speed and output power respectively. The corresponding power coefficient and tip speed ratio are shown in Figures 13 (a) and (b), respectively. In this case, the power is limited at 4 kW (rated wind speed of 9 m/s). It is clearly seen that when the wind speed is lower than 9 m/s, the output power is maximum. Conversely, if the wind speed is higher than 9 m/s, the output power will be limited at 4 kW. The control trajectory with power limit by the SMC is shown in Figure 14.

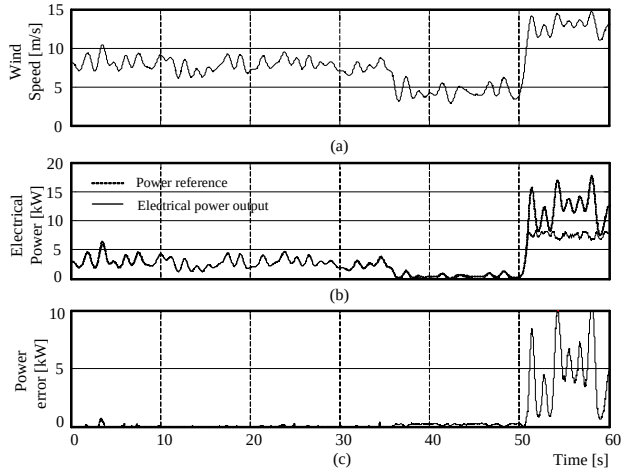

Fig. 10. a) Wind speed, b) Reference and output power, c) Power error.

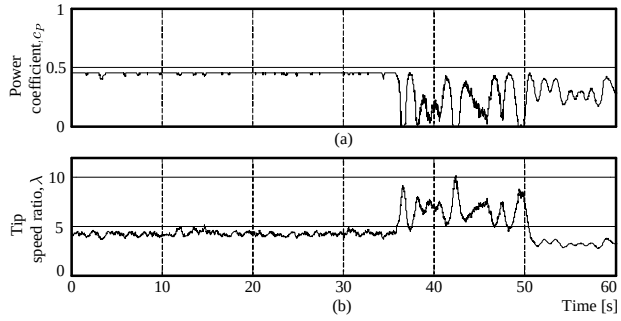

Fig. 11. a) Power coefficient, b) Tip speed ratio.

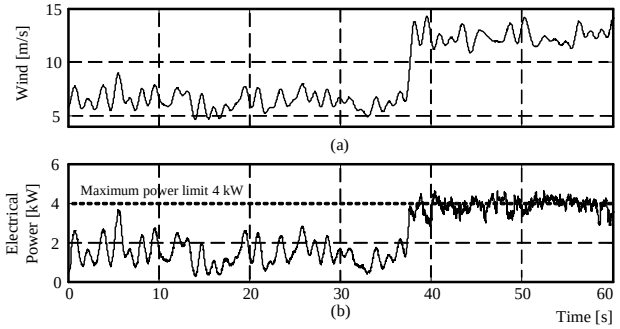

Fig. 12. a) Below rated and above rated wind speed, b) Output power with power limit at 4kW.

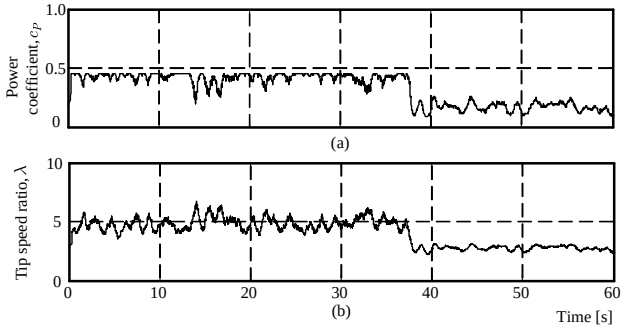

Fig. 13. a) Power coefficient, b) Tip speed ratio at 4kW.

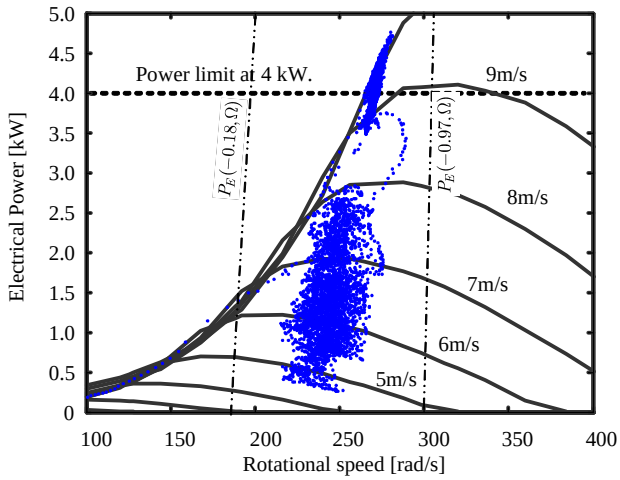

Fig. 14. Output power trajectory with stall regulation.

NOMENCLATURE

ρ	air density
λ	tip speed ratio
λ_O	tip speed ratio at maximum c_P
λ_l	tip speed ratio at low speed side
λ_h	tip speed ratio at high speed side
c_T	torque coefficient
c_P	power coefficient
$c_P^{\max}$	maximum power coefficient

A	area of turbine blade move in the air
v	velocity speed of wind
Ω	rotational speed of rotor
Ω_s	mechanical synchronous speed
Ω_o	the rotational speed at the operation point
ω_s	electrical synchronous speed
V_s	stator line voltage
R_S	stator resistance
R_R	rotor resistance
R_F	DC link resistance
L_{ds}, L_{dr}	*d*-axis stator and rotor leakage inductance
s	Slip per unit
α	firing angle
J	moment of inertia
T_g	generator torque
T_a	aerodynamic torque
η	power efficiency
P_E	electrical power output from generator
P_G	mechanical power input from turbine
u	cosine of firing angle
P_R	command reference power
β	positive constant gain

REFERENCES

[1] Çadirci I. and Ermiş, M. 1992. Double-output induction generator operating at subsynchronous and supersynchronous speeds: steady-state performance optimization and wind-energy recovery. *IEE Proc. C*, 139(5): 429-442.

[2] de Battista, H., Puleston, P., Mantz, R, and Christainsen, C. 2000. Sliding mode control of wind energy systems with doig: Power efficiency and torsional dynamics optimization. *IEEE Trans. Power Syst*., 15(2): 728-734.

[3] Hoffmann, R. and Mutschler, P. 2000. The Influence of Control Strategies on the Energy Capture of Wind Turbines. *IEEE Trans. Ind. App*, 2: 886–893.

[4] Thriringer, T. and Linders, J. 1993. Control by Variable Rotor Speed of a Fixed-Pitch Wind Turbine Operating in a Wide Speed Range. *IEEE Trans. Energy Con.*, 8(3): 520–526.

[5] Manwell, J.F., McGowan, J.G. and Rogers, A.L. 2004. *Wind Energy Explained*, John Wiley & Sons, West Sussex, England.

[6] de Battista, H. and Mantz, R. 2004. Dynamical variable structure controller for power regulation of wind energy conversion systems. *IEEE Trans. Energy Conv*., 19(4): 756-763.

[7] Utkin, V., Guldner, J. and Shi, J. 1999. *Sliding Mode Control in Electromechanical Systems*. London, U.K.: Taylor & Francis.

[8] Itkis, U. 1976. *Control systems of variable structure*, New York.: John Wiley & Sons.

[9] Sira-Ramirez, H. On the dynamical sliding mode control of nonlinear systems. *Int. Journal of Control*, 57(5): 1039-1061.

[10] Gopalswamy, S. and Hedrick, J.K. 1993. Tracking nonlinear non minimum phase systems using sliding control. *Int. Journal of Control*, 57(5): 1141-1158.

[11] Bose, B.K. 2001. *Modern Power Electronics and AC Drives.* Prentice Hall.

[12] Dewan, S.B., Slemon, G.R. and Straughen, A. 1984. *Power Semiconductor Drives*, John Wiley & Sons.

APPENDIX

The parameters used in simulation are provided below:

V_s	380 V
R_s	$400\,m\Omega$
R_r	$200\,m\Omega$
R_f	$10\,m\Omega$
L_{ds}	$122\,m\Omega$
L_{dr}	$37\,m\Omega$
J	7.5 Kg m^2
ρ	1.26kg/m^3
λ_O	4.5
$c_p^{\max}$	0.455
A	19.6350m^2

GMSARN International Journal
NOTES FOR AUTHORS

Editorial Policy

In the Greater Mekong Subregion, home to about 250 million people, environmental degradation - including the decline of natural resources and ecosystems will definitely impact on the marginalized groups in society - the poor, the border communities especially women and children and indigenous peoples. The complexity of the challenges are revealed in the current trends in land and forest degradation and desertification, the numerous demands made on the Mekong river - to provide water for industrial and agricultural development, to sustain subsistence fishing, for transport, to maintain delicate ecological and hydrological balance, etc., the widespread loss of biological diversity due to economic activities, climate change and its impacts on the agricultural and river basin systems, and other forms of crises owning to conflicts over access to shared resources. The *GMSARN International Journal* is dedicated to advance knowledge in energy, environment, natural resource management and economical development by the vigorous examination and analysis of theories and good practices, and to encourage innovations needed to establish a successful approach to solve an identified problem.

The *GMSARN International Journal* is a biannual journal published by GMSARN in June and December of each year. Papers related to energy, environment, natural resource management, and economical development are published. The papers are reviewed by world renowned referees.

Preparation Guidelines

1. The manuscript should be written in English and the desired of contents is: Title, Author's name, affiliation, and address; Abstract, complete in itself and not exceeding 200 words; Text, divided into sections, each with a separate heading; Acknowledgments; References; and Appendices. The standard International System of Units (SI) should be used.

2. Illustrations (i.e., graphs, charts, drawings, sketches, and diagrams) should be submitted on separate sheets ready for direct reproduction. All illustrations should be numbered consecutively and given proper legends. A list of illustrations should be included in the manuscript. The font of the captions, legends, and other text in the illustrations should be Times New Roman. Legends should use capital letters for the first letter of the first word only and use lower case for the rest of the words. All symbols must be italicized, e.g., α, θ, Q_{wt}. Photographs should be black and white glossy prints; but good color photographs are acceptable.

3. Each reference should be numbered sequentially and these numbers should appear in square brackets in the text, e.g. [1], [2, 3], [4]–[6]. All publications cited in the text should be presented in a list of full references in the Reference section as they appear in the text (not in alphabetical order). Typical examples of references are as follows:

   - **Book references** should contain: name of author(s); year of publication; title; edition; location and publisher. Typical example: [2] Baker, P.R. 1978. Biogas for Cooking Stoves. London: Chapman and Hall.
   - **Journal references** should contains: name of author(s); year of publication; article title; journal name; volume; issue number; and page numbers. For example: Mayer, B.A.; Mitchell, J.W.; and El-Wakil, M.M. 1982. Convective heat transfer in veetrough liner concentrators. Solar Energy 28 (1): 33-40.
   - **Proceedings reference** example: [3] Mayer, A. and Biscaglia, S. 1989. Modelling and analysis of lead acid battery operation. Proceedings of the Ninth EC PV Solar Conference. Reiburg, Germany, 25-29 September. London: Kluwer Academic Publishers.
   - **Technical paper** reference example: [4] Mead, J.V. 1992. Looking at old photographs: Investigating the teacher tales that novice teachers bring with them. Report No. NCRTL-RR-92-4. East Lansing, MI: National Center for Research on Teacher Learning. (ERIC Document Reproduction Service No. ED346082).
   - **Online journal** reference example: [5] Tung, F. Y.-T., and Bowen, S. W. 1998. Targeted inhibition of hepatitis B virus gene expression: A gene therapy approach. Frontiers in Bioscience [On-line serial], 3. Retrieved February 14, 2005 from http://www.bioscience.org/1998/v3/a/tung/a11-15.htm.

4. Manuscript can be uploaded to the website or sent by email. In case of hard copy, three copies of the manuscript should be initially submitted for review. The results of the review along with the referees' comments will be sent to the corresponding author in due course. At the time of final submission, one copy of the manuscript and illustrations (original) should be submitted with the diskette. Please look at the author guide for detail.

GMSARN Members

Asian Institute of Technology

Hanoi University of Technology

Ho Chi Minh City University of Technology

Institute of Technology of Cambodia

Khon Kaen University

Kunming University of Science and Technology

National University of Laos

Royal University of Phnom Penh

Thammasat University

Yangon Technological University

Yunnan University

Guangxi University

Published by the **Greater Mekong Subregion Academic and Research Network (GMSARN)**
c/o Asian Institute of Technology (AIT)
P.O. Box 4, Klong Luang
Pathumthani 12120, Thailand
Tel: (66-2) 524-5437; Fax: (66-2) 524-6589
E-mail: gmsarn@ait.ac.th
Website: http://www.gmsarn.org